
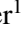









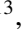



The CARMENES search for exoplanets around M dwarfs

Wolf 1069 b: Earth-mass planet in the habitable zone of a nearby, very low-mass star[★]

D. Kossakowski¹, M. Kürster¹, T. Trifonov^{1,2}, Th. Henning¹, J. Kemmer³, J. A. Caballero⁴, R. Burn¹, S. Sabotta³, J. S. Crouse^{5,6,7,★★}, T. J. Fauchez^{5,8,★★}, E. Nagel^{9,10}, A. Kaminski³, E. Herrero^{11,12}, E. Rodríguez¹³, E. González-Álvarez¹⁴, A. Quirrenbach³, P. J. Amado¹³, I. Ribas^{11,12}, A. Reiners¹⁵, J. Aceituno^{16,13}, V. J. S. Béjar^{17,18}, D. Baroch^{11,12}, S. T. Bastelberger^{6,5,7,★★}, P. Chaturvedi¹⁰, C. Cifuentes⁴, S. Dreizler¹⁵, S. V. Jeffers¹⁹, R. Kopparapu^{5,★★}, M. Lafarga^{20,11,12}, M. J. López-González¹³, S. Martín-Ruiz¹³, D. Montes²¹, J. C. Morales^{11,12}, E. Pallé^{17,18}, A. Pavlov¹, S. Pedraz¹⁶, V. Perdelwitz^{22,9}, M. Pérez-Torres^{13,23}, M. Perger^{11,12}, S. Reffert³, C. Rodríguez López¹³, M. Schlecker^{24,1}, P. Schöfer^{13,15}, A. Schweitzer⁹, Y. Shan^{25,15}, A. Shields²⁶, S. Stock³, E. Wolf^{27,5,28}, M. R. Zapatero Osorio¹⁴, and M. Zechmeister¹⁵

(Affiliations can be found after the references)

Received 28 October 2022 / Accepted 21 December 2022

ABSTRACT

We present the discovery of an Earth-mass planet ($M_p \sin i = 1.26 \pm 0.21 M_\oplus$) on a 15.6 d orbit of a relatively nearby ($d \sim 9.6$ pc) and low-mass ($0.167 \pm 0.011 M_\odot$) M5.0 V star, Wolf 1069. Sitting at a separation of 0.0672 ± 0.0014 au away from the host star puts Wolf 1069 b in the habitable zone (HZ), receiving an incident flux of $S = 0.652 \pm 0.029 S_\oplus$. The planetary signal was detected using telluric-corrected radial-velocity (RV) data from the CARMENES spectrograph, amounting to a total of 262 spectroscopic observations covering almost four years. There are additional long-period signals in the RVs, one of which we attribute to the stellar rotation period. This is possible thanks to our photometric analysis including new, well-sampled monitoring campaigns undergone with the OSN and TJO facilities that supplement archival photometry (i.e., from MEarth and SuperWASP), and this yielded an updated rotational period range of $P_{\text{rot}} = 150\text{--}170$ d, with a likely value at $169.3^{+3.7}_{-3.6}$ d. The stellar activity indicators provided by the CARMENES spectra likewise demonstrate evidence for the slow rotation period, though not as accurately due to possible factors such as signal aliasing or spot evolution. Our detectability limits indicate that additional planets more massive than one Earth mass with orbital periods of less than 10 days can be ruled out, suggesting that perhaps Wolf 1069 b had a violent formation history. This planet is also the sixth closest Earth-mass planet situated in the conservative HZ, after Proxima Centauri b, GJ 1061 d, Teegarden's Star c, and GJ 1002 b and c. Despite not transiting, Wolf 1069 b is nonetheless a very promising target for future three-dimensional climate models to investigate various habitability cases as well as for sub- $m s^{-1}$ RV campaigns to search for potential inner sub-Earth-mass planets in order to test planet formation theories.

Key words. methods: data analysis – planetary systems – stars: individual: Wolf 1069 – stars: low-mass – techniques: radial velocities

1. Introduction

An impressive 5000 exoplanets and counting have been detected thus far¹, largely thanks to the past and ongoing radial-velocity (RV) and transit surveys. On the hunt for an Earth analog, out of these thousands of planets, only ~ 50 have been found to sit in the so-called habitable zone (HZ) of their stellar host², which

is defined to be the circumstellar region in which liquid water could potentially exist on the surface of the planet (Kasting et al. 1993; Kopparapu et al. 2013). Only 20 of these are considered to be Earth-sized, defined by radii of $0.8 R_\oplus < R_p < 1.6 R_\oplus$ or by masses of $0.5 M_\oplus < M \sin i_p < 3 M_\oplus$. Moreover, a majority of them have been discovered around M-dwarf stellar hosts, most likely due to the ease in detectability considering the higher planet-to-star mass and radius ratios (see e.g., Zechmeister et al. 2009; Seager 2010; Bonfils et al. 2013; Shields et al. 2016; Perryman 2018).

The definition of the HZ is not a definite implication for a life-hosting world, but rather acts as a good indicator for a planet to show further promising potential for markers of surface habitability. There are in fact a variety of factors that affect its habitability potential, such as the X-ray/UV emission or age in regards to the stellar host, or processes due to the planet itself including its atmospheric composition or its ability to retain certain elements in its atmosphere (e.g., Dong et al. 2018;

^{*} Full Table D.2 and additional data (i.e., stellar activity indicators as shown in Fig. 4 and long-term photometry as in Fig. 2) are only available at the CDS via anonymous ftp to cdsarc.cds.unistra.fr (130.79.128.5) or via <https://cdsarc.cds.unistra.fr/viz-bin/cat/J/A+A/670/A84>

^{**} NASA GSFC Sellers Exoplanet Environments Collaboration.

¹ <https://exoplanetarchive.ipac.caltech.edu/>, accessed on 16 September 2022.

² The Habitable Exoplanet Catalog: <http://phl.upr.edu/projects/habitable-exoplanets-catalog>, last updated on 6 December 2021 and further discussed in Appendix B.

Kopparapu et al. 2020). For this reason, it is not only crucial to first gather planets that are situated within the HZ, but also, it is necessary to build a better understanding of the stellar effects on the planet's habitability (e.g., Segura et al. 2003, 2010; Hilton 2011; Cohen et al. 2014; Chadney et al. 2016), and to also characterize its atmosphere observability, with instruments such as the *James Webb* Space Telescope (JWST; Gardner et al. 2009).

Even though most HZ planets around low-mass M dwarfs are RV-only detections that do not transit, we can nonetheless generate useful indicators to investigate their habitability further. Three-dimensional (3D) general circulation model (GCM) climate simulations (e.g., Way et al. 2017; Wolf et al. 2022) can produce predictions to investigate various atmosphere compositions to test how durably habitable the planet is. These analyses, along with a push for improvements in thermal emission and reflected light phase curve observations, are crucial given the rise of nontransiting planets found in the HZ of stellar hosts within the solar neighborhood (e.g., Anglada-Escudé et al. 2016; Dreizler et al. 2020).

In this paper, we turn our attention to the discovery of Wolf 1069 b, an Earth-mass planetary companion orbiting a mid-type M dwarf within the conservative HZ limits, as defined by Kopparapu et al. (2013). This planet could very well possess the key factors in making it indeed a habitable world according to preliminary 3D GCM models. Also, in contrast to other habitable worlds in the conservative HZ with similar host stars (i.e., Kepler-1649, Proxima Centauri, GJ 1061, Teegarden's Star, and GJ 1002), Wolf 1069 b is the only one within the conservative HZ without an inner planet, based on our current detection limits. This notion is supported by the works of Burn et al. (2021), Mulders et al. (2021), and Schlecker et al. (2021), where we expect a lower planet occurrence rate for stars with $M_{\star} < 0.2 M_{\odot}$ than for stars with $0.2 M_{\odot} < M_{\star} < 0.5 M_{\odot}$ for both the pebble and core accretion scenarios. Granted, these are theoretical predictions as more observation-based evidence is required to confirm this, and Wolf 1069 b could still be accompanied by closer-in and outer planets. Nevertheless, the concept that only one planet survives is predicted by formation models if there were at least one giant impact at the late stage. This would enhance the chance of having a massive moon similar to the Earth and might also stir up the interior of the planet to prevent stratification and sustain a magnetic field (e.g., Jacobson et al. 2017). As remote as this appears, the search for exo-moons is no longer so far-fetched in recent times (e.g., Martínez-Rodríguez et al. 2019; Dobos et al. 2022).

The paper is outlined as follows. Section 2 first presents the comprehensive spectroscopic and photometric data collected for this work. Then, the host star and its properties are introduced in Sect. 3, in which we determine and update its rotational period using newly taken photometry from our facilities. The various signals in the RVs for this system are investigated and modeled in Sect. 4, where the results and prospects for Wolf 1069 b are then discussed in Sect. 5. We finally display our conclusions in Sect. 6.

2. Observational data

2.1. CARMENES high-resolution spectroscopy

The CARMENES³ instrument is located at the 3.5 m telescope at the Calar Alto Observatory in Spain and consists of two separate spectrographs residing in two channels: the visual

³ Calar Alto high-Resolution search for M dwarfs with Exo-earths with Near-infrared and optical Échelle Spectrographs, <http://carmenes.caha.es>

(VIS), which covers the spectral range 520–960 nm (spectral resolution of $\mathcal{R} = 94\,600$), and the near-infrared (near-IR), which covers the 960–1710 nm range ($\mathcal{R} = 80\,400$; Quirrenbach et al. 2014, 2018). Wolf 1069 (Karmn J20260+585) was one of the ~300 stars initially chosen as part of the CARMENES Guaranteed Time Observation (GTO) program (Reiners et al. 2018), and 276 observations were since accumulated spanning 1450 days (June 2016–June 2020). There were six measurements that were missing a drift correction as well as an additional eight that had low signal-to-noise ratio, and were, for this reason, discarded, resulting in 262 usable RV measurements. Furthermore, the spectra were notably affected by telluric absorption (e.g., Reiners et al. 2018). We corrected them by employing the template division telluric modeling methodology, a technique to remove telluric absorption lines from stellar spectra with numerous intrinsic lines (Nagel et al. 2022). This technique is suitable for separating telluric and spectral components based on the Earth's barycentric motion throughout the year. The telluric-free spectra of Wolf 1069 are then produced by fitting a synthetic transmission model of the Earth's atmosphere to each individually extracted telluric spectrum with *molecfit* (Smette et al. 2015). The weighted root mean square (wrms) and the median uncertainty of the remaining 262 data points are 2.66 m s^{-1} and 1.67 m s^{-1} , respectively. The simultaneously taken near-IR measurements were not considered as part of the analysis given the notably higher wrms of 7.0 m s^{-1} along with the significantly higher mean uncertainty of each observation. Therefore, we continue the analysis with the 262 telluric-absorption-corrected VIS spectra. The CARMENES RV data with their uncertainties are displayed in the top panel of Fig. 1.

The raw data are first pipelined through the standard guaranteed time observations via *caracal* (Caballero et al. 2016b). Then, the RVs are determined using *serval*⁴ (Zechmeister et al. 2018), where the spectra are corrected for barycentric motion, secular acceleration, and instrumental drift, and then nightly zero-points were calculated and applied (Trifonov et al. 2020). In addition, *serval* produces various stellar activity indicators such as the chromatic index (CRX), the differential line width (dLW), the $H\alpha$ index, the Ca II IR triplet (IRT) lines, and the Na I D doublet lines. We also obtained the photospheric absorption band indices TiO λ 7050 Å, TiO λ 8430 Å, and TiO λ 8860 Å from the nontelluric-corrected spectra using spectral ranges without notable telluric contamination, as defined by Schöfer et al. (2019). Lastly, we computed the cross-correlation function (CCF) and its full-width half-maximum (FWHM), contrast (CTR), and bisector velocity span (BVS) values computed with the *raccoon*⁵ code, adopting the approach of using binary masks as explained in Lafarga et al. (2020). These indicators were investigated for the rotation period of the stellar host (Sect. 3.2).

2.2. Our photometric campaigns

We carried out simultaneous, continuous photometric follow-up of Wolf 1069 from 2017 to 2020 with the photometric facilities as listed below. A summary of the various photometric data sets is found in Table 1. They are also displayed as a time series in Fig. 2.

Observatorio de Sierra Nevada (OSN). The Observatorio de Sierra Nevada (OSN)⁶, currently maintained by the Instituto de Astrofísica de Andalucía (IAA) and situated at Loma de Dilar

⁴ <https://github.com/mzechmeister/serval>

⁵ <https://github.com/mlafarga/raccoon>

⁶ <https://www.osn.iaa.csic.es/en>

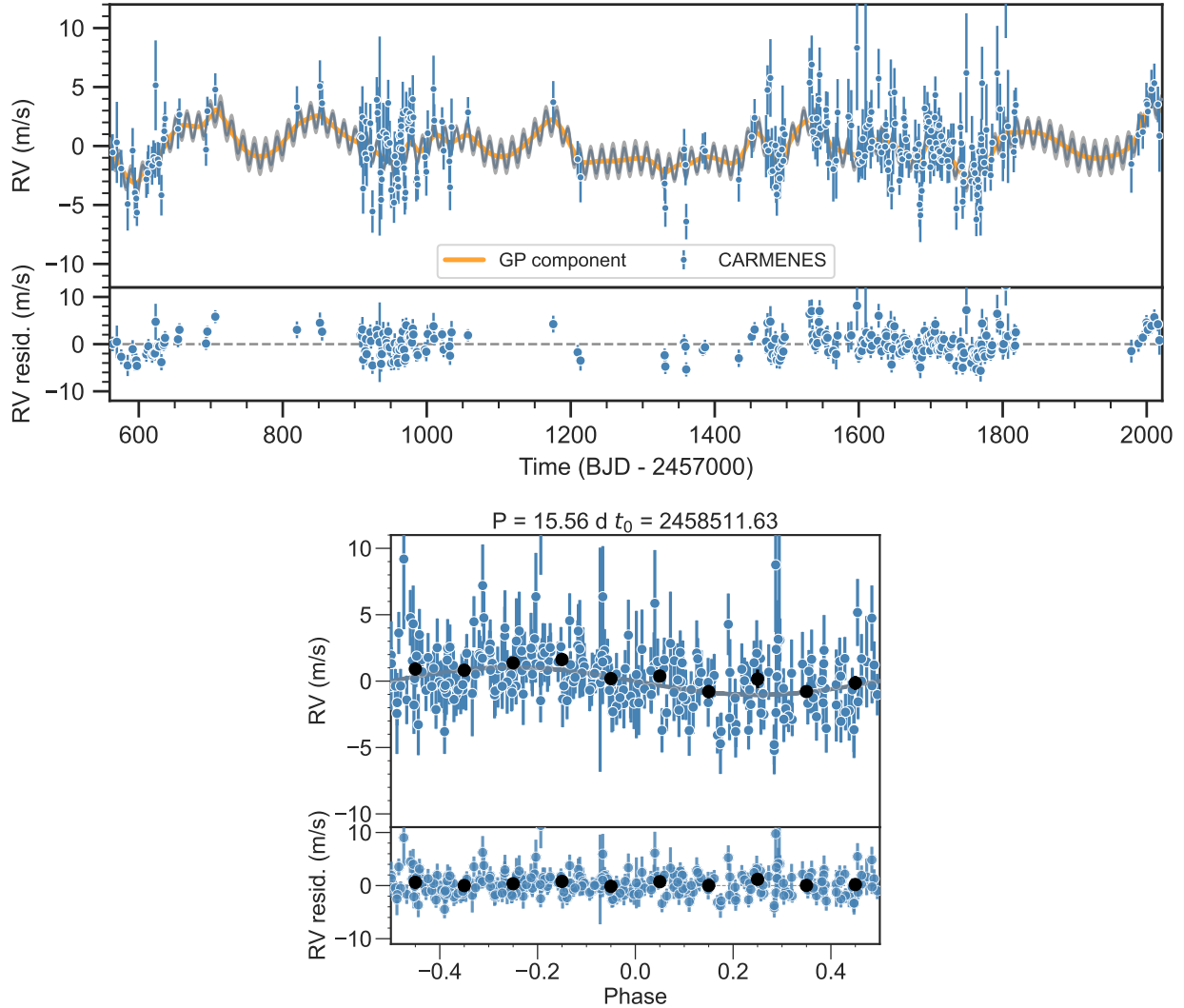


Fig. 1. RV time series and phase-folded plots for Wolf 1069 b. Top panel: CARMENES VIS RV measurements for Wolf 1069 along with the best-fit model (dark gray line) and the stellar rotation period modeled by a dSHO-GP (orange). The light gray band indicates the 68% confidence interval of the model. Bottom panel: RVs phase-folded to the period of Wolf 1069 b at 15.6 d ($K_b = 1.07 \pm 0.17 \text{ m s}^{-1}$) and with the GP component subtracted out. The black circles represent the data points binned to 0.1 in phase space for visualization purposes. The bottom panel for each plot represents the residuals after subtracting out the model. There are two data points that did not fit within the boundary for visual reasons.

in Granda, Spain, hosts two Nasmyth optical telescopes with apertures of 90 cm (T90) and 150 cm (T150). Both telescopes are equipped with similar VersArray $2k \times 2k$ CCD cameras, which deliver images with fields of view (FOV) of $13.2 \text{ arcmin} \times 13.2 \text{ arcmin}$ (T90; Amado et al. 2021) or $7.92 \text{ arcmin} \times 7.92 \text{ arcmin}$ (T150; Rodríguez et al. 2010). Each camera is based on a high quantum efficiency back-illuminated CCD chip, type Marconi-EEV CCD42-4, with optimized response in the ultraviolet. We monitored Wolf 1069 using both telescopes and various observing runs between the years 2017 and 2020. The observations with the T90 telescope were collected using both Johnson *V* and *R* filters during three observing runs as tabulated in Table 1. Each epoch typically consisted of 20 exposures of 80 s in each filter per night. The resulting light curves were obtained by the method of synthetic aperture photometry. Each CCD frame was corrected in a standard way for bias and flat-fielding. Different aperture sizes were tested in order to choose the best one for our observations. A number of nearby and relatively bright stars within the frames were selected as reference stars to produce differential photometry of Wolf 1069. Outliers due to poor observing conditions or very high airmass were removed.

The observations with the T150 telescope were collected during a single observing run and were reduced in the same way. In this case, each epoch typically consisted of 30 exposures of 80 s, 35 s, and 10 s in each *V*, *R*, and *I* filter, respectively, per night.

Telescopi Joan Oró (TJO). Simultaneous to the OSN photometry, observations for Wolf 1069 were carried out with the 80 cm TJO⁷ at the Observatori del Montsec in Lleida, Spain. The images were obtained with an exposure time of 60 seconds using the Johnson *R* filter of the LAIA imager, a $4k \times 4k$ CCD with a FOV of 30 arcmin and a plate scale of 4 arcsec/pixel. The images were calibrated with darks, bias, and flat fields with the ICAT pipeline (Colome & Ribas 2006) of the TJO. The differential photometry was extracted with AstroImageJ (Collins et al. 2017) using the aperture size that minimized the rms of the resulting relative fluxes, and a selection of the 20 brightest comparison stars in the field, which did not show variability. Then, data points with a low S/N were filtered from the light curve, and any points with relative fluxes greater than 1.08 or less than 0.96 were removed before nightly binning.

⁷ <http://www.ieec.cat/content/206/what-s-the-oadm/>

Table 1. Observing log of ground-based long-term photometric observations acquired for Wolf 1069.

Instrument	Date		Filter	$\Delta t^{(a)}$ (d)	N_{obs}	$N_{\text{nights}}^{(b)}$	rms ^(c) (ppt)	
	Begin	End						
SuperWASP	13 June 2007	12 August 2008	400–700 nm	426	10 436	172	10.05	
MEarth-tel01	29 September 2012	08 July 2015	} RG715	1 012	2 595	183	6.02	
	13 September 2017	19 November 2018		431	6 237	177	6.85	
MEarth-tel05	28 May 2012 [†]	10 November 2015 [†]		1 260	2 716	228	5.44	
	13 September 2017	19 November 2018		431	5 665	175	6.52	
OSN-T150	31 August 2017	06 December 2017		V	97	1 322	41	8.65
	31 August 2017	06 December 2017		R	97	1 276	39	5.90
	14 September 2017	06 December 2017	I	84	1 078	37	6.38	
OSN-T90	29 June 2017	04 September 2017	} V	67	439	24	6.07	
	21 June 2019	29 October 2019		130	719	45	7.42	
	26 June 2020	02 November 2020		129	1187	64	8.73	
	29 June 2017	04 September 2017	} R	67	442	24	5.68	
	21 June 2019	29 October 2019		130	716	45	8.10	
	26 June 2020	02 November 2020		129	1207	64	6.40	
TJO-T80	19 December 2018	12 January 2020	R	388	1 345	79	10.02	

Notes. ^(a)Time span of the observation. ^(b)Number of nightly binned observations. ^(c)Root mean square in parts-per-thousand. Data sets that were not used for the photometric rotational period determination are indicated by a dagger [†].

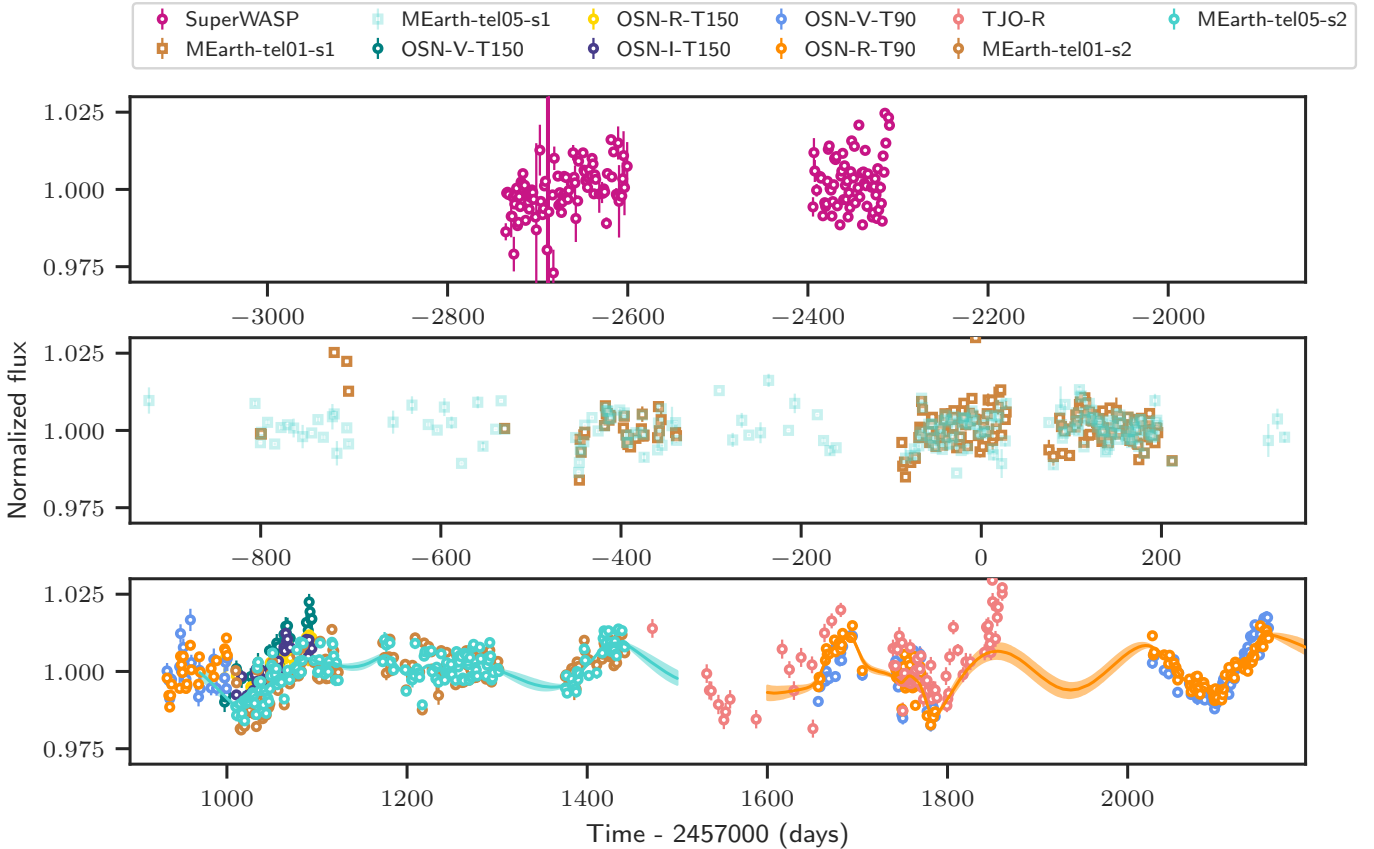


Fig. 2. Time series of the long-term photometry for Wolf 1069 color coded by instrument and filter. The time range for each panel is consistent among all panels. The MEarth-tel05-s1 data were not included in the final rotational period determination but are faintly shown for illustrative purposes. Given that the GP model is unique to each instrument with its own amplitude hyperparameter (see for example Fig. 8 in Kemmer et al. 2020), the extrapolated GP models of two instruments (MEarth-tel-05 and OSN-R-T90) are overplotted with the same color as their respective data sets for illustrative purposes.

2.3. Photometric monitoring surveys

Additionally, we compiled a collection of archival long-term photometric data taken by monitoring surveys as described below. They are also listed in Table 1 and illustrated in Fig. 2.

SuperWASP. The SuperWASP⁸ project is led by a chiefly UK-based consortium. Using two arrays of robotic telescopes operating in the northern and southern hemispheres, the survey obtains light curves for millions of objects at high cadence to look for transiting planets and study other astrophysical phenomena across the entire sky (Pollacco et al. 2006; Butters et al. 2010). SuperWASP-North is located at the Roque de los Muchachos Observatory in La Palma, whereas SuperWASP-South is at the South African Astronomical Observatory near Sutherland, South Africa. Each observatory consists of eight wide-angle cameras with Canon 200 mm, f/1.8 lenses that feed into 2048 × 2048 CCDs. The pixel scale is 13.7 arcsec.

Wolf 1069 was monitored for four seasons with SuperWASP-North from 2007 to 2010, though only sparsely in the last two seasons. The usable data spans from June 2007 to August 2008 with a ~6 month gap. We received the complete light curve, corrected for instrumental and atmospheric systematics, from the SuperWASP team. The detrending procedure is nonaggressive and expected to preserve true astrophysical signals (including rotational modulation), as documented by Tamuz et al. (2005). After clipping the final two seasons and iteratively rejecting outliers commensurate with the size of the data set in each season, we binned the data nightly such that the weighted mean and error of all the data points that go into each bin constitutes the flux and error of that bin.

MEarth-North. Wolf 1069 was observed by the MEarth⁹ project (Irwin et al. 2015), specifically with the MEarth-North array composed of eight 40 cm telescopes, each equipped with a 25.6 arcmin × 25.6 arcmin FOV Apogee U42 camera, and located at the Fred Lawrence Whipple Observatory on Mount Hopkins nearby Tucson, Arizona, USA. Using the light curves from the latest data release¹⁰, the target was observed for more than six years with telescope one (“MEarth-tel01”) and telescope five (“MEarth-tel05”). The MEarth project generally uses a RG715 long-pass filter, except for the 2010–2011 season when an I_{715–895} interference filter was chosen. In the case of Wolf 1069, with observations collected from both telescopes later than October 2011, the RG715 filter was always used, and thus, we consider each photometric light curve as its own. The data were nightly binned following the same procedure as for the SuperWASP data. Particularly for first season with MEarth-tel05, we excluded certain nightly measurements where only one observation was taken to ensure accurate data quality. This constituted ~15 nights out of the final 228 (Table 1), which were in the end not considered for the final rotational period determination due to large noisiness (see Sect. 3.2).

TESS. Wolf 1069 was thus far observed in three of the northern sectors (15 – camera #2 CCD #4; 16 – camera #2 CCD #3; 17 – camera #3 CCD #4, 15 August – 2 November 2019) during the nominal mission of the Transiting Exoplanet Survey Satellite (TESS; Ricker et al. 2015) with the short 2-minute cadence photometry, as well as in three sectors (41 – camera #2 CCD #1; 23 July 2021 – 20 August 2021, 55 – camera #3 CCD

#3; 05 August 2022 – 01 September 2022; 56 – camera #3 CCD #3; 01 September 2022 – 30 September 2022) during the extended mission with 2-min and 20-sec cadence¹¹. The target is being currently observed in one sector (57 – camera #3 30 September 2022 – 29 October 2022). The publicly available data from all sectors were downloaded from the Mikulski Archive for Space Telescopes¹². Following the typical procedure, these data are corrected for artifacts and systematic trends (Pre-search Data Conditioning, PDC_SAP flux – Smith et al. 2012; Stumpe et al. 2012, 2014), provided by the Science Processing Operations Center (SPOC; Jenkins et al. 2016). We use these data for our analysis.

3. Stellar properties

3.1. Basic astrophysical properties

Wolf 1069 (GJ 1253, Karmn J20260+585) is a slowly rotating, high-proper motion M5.0 V star at less than 10 pc discovered by Wolf (1920). For decades, it was the subject only of astrophotometric analysis of stars in the solar neighborhood (Luyten 1955; Gliese & Jahreiß 1979; Probst 1983; Weis 1984), with the first spectral analysis by Bidelman (1985). Since the end of the 20th century, Wolf 1069 was more investigated in X-rays (Wood et al. 1994; Stelzer et al. 2013), with high-resolution imaging (Dieterich et al. 2012; Jódar et al. 2013; Janson et al. 2014; Lamman et al. 2020), and especially for determining its astrophysical stellar parameters (Rojas-Ayala et al. 2012; Mann et al. 2015; Rajpurohit et al. 2018; Marfil et al. 2021).

We summarize the stellar properties of Wolf 1069 in Table 2. Following Cifuentes et al. (2020), we integrated the spectral energy distribution and computed the bolometric luminosity using broadband photometry and the latest parallactic distance from Gaia Data Release 3 (DR3; Gaia Collaboration 2023). From this value and the effective temperature of the star, determined spectroscopically by Passegger et al. (2019), we derived the radius from the Stefan-Boltzmann law, and the mass from the mass-radius relation by Schweitzer et al. (2019). All tabulated parameters agree within uncertainties with published values (e.g., Jenkins et al. 2009; Terrien et al. 2015; Lafarga et al. 2020), except for the rotation period, which we concluded to be 150–170 d. Our P_{rot} determination is explained in detail and compared with the literature in Sect. 3.2. Although Wolf 1069 kinematically belongs to the Galactic thin disk (i.e., younger ages of ~1–5 Gyr) according to the galactocentric velocities calculated as in Montes et al. (2001) with a custom made python code (Cortés-Contreras et al., in prep.), the very long P_{rot} determined by us points toward older ages (~7–11 Gyr; Newton et al. 2016). The low activity indicators (H α and X-ray emission) and slow rotational velocity, $v \sin i$, are also in line with a long P_{rot} . As a result, Wolf 1069 is a very weakly active star, which facilitates the identification of RV signals with very low semi-amplitudes.

3.2. Stellar rotation period

Using MEarth light curves from 2011 to 2014, Díez Alonso et al. (2019) determined a photometric rotation period of 57.7 d for Wolf 1069. However, the same data were analyzed earlier by Newton et al. (2016), who reported only a tentative signal at 142.1 d and noted that it did not meet their criteria for a confident detection. To further establish the stellar rotation period, we

⁸ Super-Wide Angle Search for Planets.

⁹ <https://www.cfa.harvard.edu/MEarth/Welcome.html>

¹⁰ DR10: <https://1web.cfa.harvard.edu/MEarth/DR10/north2011-2020/>

¹¹ <https://heasarc.gsfc.nasa.gov/cgi-bin/tess/webtess/wtv.py>

¹² <https://mast.stsci.edu>

Table 2. Stellar parameters of Wolf 1069.

Parameter	Value	Reference
<i>Basic identifiers and data</i>		
Name	Wolf 1069	Wolf1920
GJ	1253	Gli57
Karmn	J20260+585	Cab16
<i>Gaia</i> DR3	2188318517720321664	<i>Gaia</i> DR3
<i>G</i> (mag)	12.352 ± 0.003	<i>Gaia</i> DR3 ^(a)
<i>Coordinates and spectral classification</i>		
α (ICRS)	20:26:05.80	<i>Gaia</i> DR3
δ (ICRS)	+58:34:31.4	<i>Gaia</i> DR3
Sp. type	M5.0 V	Reid95
<i>Parallax and kinematics</i>		
π (mas)	104.441 ± 0.026	<i>Gaia</i> DR3
<i>d</i> (pc)	9.5747 ± 0.0024	<i>Gaia</i> DR3
$\mu_\alpha \cos \delta$ (mas yr ⁻¹)	261.038 ± 0.032	<i>Gaia</i> DR3
μ_δ (mas yr ⁻¹)	542.906 ± 0.031	<i>Gaia</i> DR3
γ (km s ⁻¹)	-60.047 ± 0.020	Lafa20
<i>U</i> (km s ⁻¹)	-23.1335 ± 0.0057	This work
<i>V</i> (km s ⁻¹)	-61.2071 ± 0.0200	This work
<i>W</i> (km s ⁻¹)	-8.4689 ± 0.0060	This work
Galactic population	Thin disk	This work
<i>Photospheric parameters</i>		
<i>T</i> _{eff} (K)	3158 ± 54	Pass19
log <i>g</i> _★ (cgs)	4.93 ± 0.06	Pass19
[Fe/H] (dex)	0.07 ± 0.19	Pass19
<i>v</i> sin <i>i</i> _★ (km s ⁻¹)	<2	Rein18
pEW(H α)	-0.045 ± 0.082	Fuhr22
$\langle B \rangle$ (G)	<620	Rein22
log <i>F</i> _X (mW m ⁻²)	-13.27	Stel13
<i>P</i> _{rot} (d)	150–170	This work ^(b)
<i>Physical parameters</i>		
<i>L</i> _★ (10 ⁻⁴ <i>L</i> _☉)	29.44 ± 0.28	This work
<i>R</i> _★ (<i>R</i> _☉)	0.1813 ± 0.0063	This work
<i>M</i> _★ (<i>M</i> _☉)	0.167 ± 0.011	This work
Conservative HZ (au) ^(c)	[0.056,0.111]	This work

Notes. ^(a)See Table D.1 for multiband photometry different from *Gaia* DR3 *G* band. ^(b)See Sect. 3.2 for the *P*_{rot} determination. ^(c)For planets with *M*_p = 1 *M*_⊕.

References. Cab16: Caballero et al. (2016a); Cif20: Cifuentes et al. (2020); *Gaia* DR3: *Gaia* Collaboration (2023); Fuhr20: Fuhrmeister et al. (2020); Fuhr22: Fuhrmeister et al. (2022); Gli57: Gliese (1957); Lafa20: Lafarga et al. (2020); Mar21: Marfil et al. (2021). Pas19: Passegger et al. (2019); Reid95: Reid et al. (1995); Rein22: Reiners et al. (2022); Schw19: Schweitzer et al. (2019); Stel13: Stelzer et al. (2013); Wolf1920: Wolf (1920).

examined all available photometric measurements, including the newer-taken observations from the OSN and TJO telescopes, along with various stellar activity indicators available from the CARMENES spectra.

Long-term photometry. Considering each photometric data set alone, namely, OSN, TJO, SuperWASP, and MEarth, all indicate hints toward a prominent peak of ~150–165 d when taking a look at the generalized Lomb-Scargle (GLS; Zechmeister & Kürster 2009) periodograms, along with strong peaks present at

the respective alias frequencies (Fig. 3). Interestingly, while this periodicity does present itself significantly in most photometric data sets, the most prominent peak in some is rather at a longer period (~200–300 d), which can also be connected to an alias signal of the presumed rotational period due to the sampling for each of the respective data sets. Focusing on the first season of the photometry from MEarth, solely from tel-01 as the data from tel-05 are rather noisy, the highest peak is around 140 d, similar to Newton et al. (2016). On the other hand, the second observing block of the MEarth data, considering now data from both the tel-01 and tel-05 instruments, peaks clearly at ~158 d, with present alias signals (i.e., ~110 d and ~300 d) due to the sampling of 320 d.

To determine the rotational period of Wolf 1069, we performed a fit with juliet¹³ (Espinoza et al. 2019) using the sum of two stochastically driven, damped harmonic oscillator (SHO) terms, or a double SHO Gaussian process (dSHO-GP), as done so in previous works such as, David et al. (2019), Gillen et al. (2020), and Kossakowski et al. (2021) first considering all the data sets. A summary of the priors used for the analysis is found in Table C.1. To set this up, we treated the OSN data as effectively different instruments arranged together only if the telescope size (i.e., T90 and T150) and filter (i.e., *V*, *R*, and *I*) were the same across multiple observational seasons. Each telescope of the MEarth data were separated into two temporal subsets, namely MEarth-tel05-s1 and MEarth-tel05-s2, and the same for MEarth-tel01 though without tel05, to account for possible changes in stellar activity behavior over long periods of time (i.e., ~800 d). The SuperWASP data were kept as is. We imposed a log-uniform prior for the rotational period, *P*_{rot}, shared among all instruments ranging from 10 d to 200 d to avoid samples from populating near the longer-period alias signal. Likewise, the quality factor for the secondary oscillation, *Q*₀, and the difference between the quality factors of the first and second oscillations, δQ , were also shared. As for the fractional amplitude of the secondary oscillation with respect to the primary one, *f*, this parameter was shared among instruments with the same filter, that is, wavelength. The amplitude of the dSHO-GP, σ_{GP} , followed suit as the dSHO-GP is trying to model the underlying physical behavior of the star that is wavelength dependent. To then account for any individual instrumental systematics, each respective instrument had its own offset value and jitter term¹⁴ (Baluev 2009).

From the posterior results of this fit, we obtain a rotational period of 169.3^{+3.7}_{-3.6} d, compatible with the peaks in the periodograms and their widths (Fig. 3). To further experiment, we also tested out the same model setup, but this time solely on the photometry contemporaneously taken with the RVs, meaning those data comprising the last panel of Fig. 2. The reason for considering just these data is that, it could be possible that the star underwent some changes in activity on the long scale due to spot migration or differential rotation. The results of this run give a rotational period of 170⁺¹⁵₋₁₁ d, which is 1 σ well in agreement when considering all photometry, ensuring that the behavior of the star is still applicable to today. Therefore, we determine the photometric stellar rotation period to be 169.3^{+3.7}_{-3.6} d.

Spectroscopy. We furthermore explored the various stellar activity indicators provided by the CARMENES spectra as

¹³ <https://juliet.readthedocs.io/en/latest/index.html>

¹⁴ The jitter term is an additional noise count that is added in quadrature to the nominal uncertainty values.

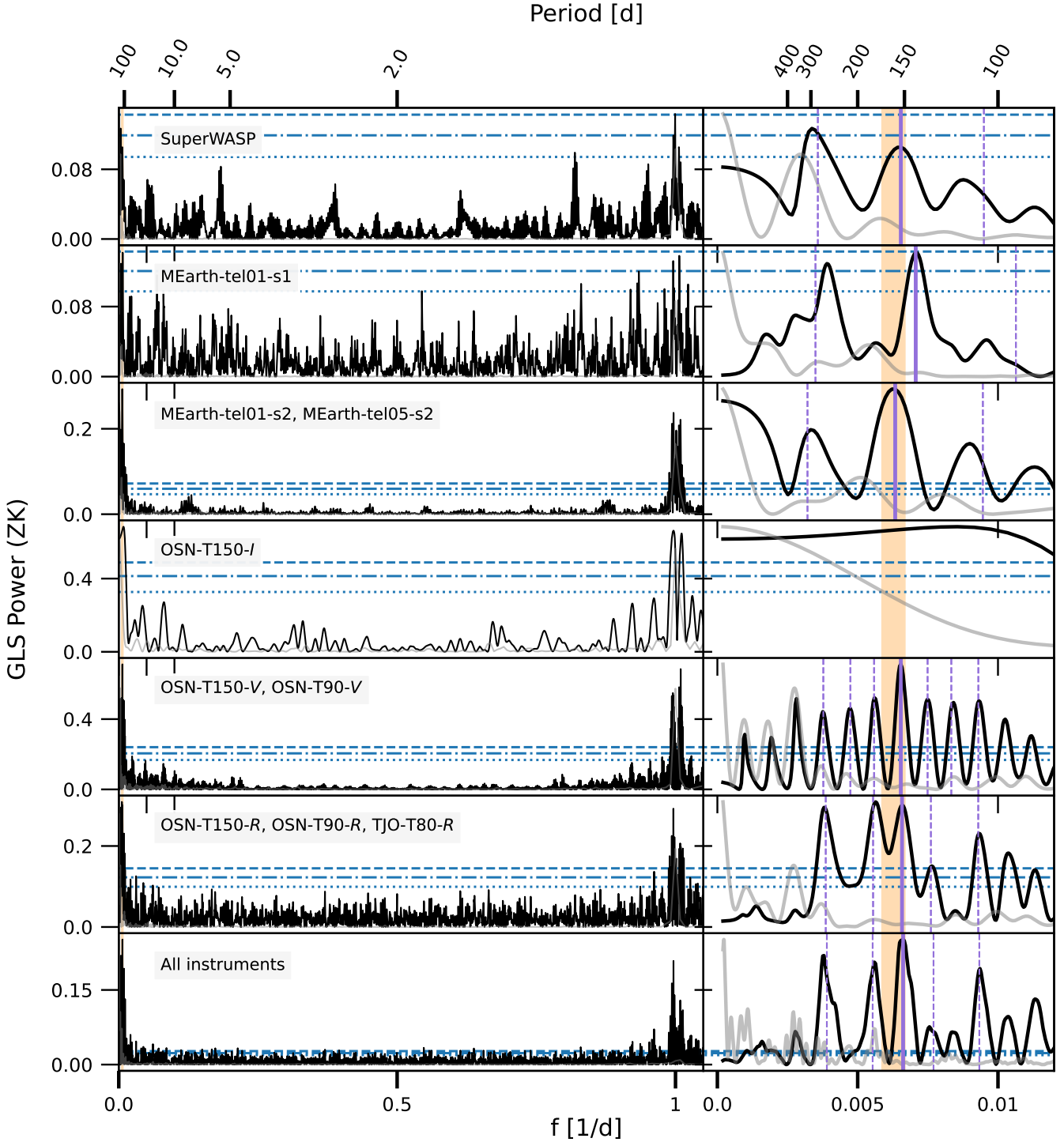


Fig. 3. GLS periodograms for the long-term photometric data of Wolf 1069. The right panels are zoomed in to the longer-period regime. Each horizontal panel represents an effective instrument that was considered for the determination of the stellar rotation period (Sect. 3.2). The normalized GLS power of the sampling of the data for each row is shown in gray. The range for the photometric rotation period of 150–170 d is shaded in orange. Some significant alias signals due to the sampling of each respective data set are illustrated with a vertical dashed line, whereas the true signal is marked with a solid line.

well as the RVs themselves to look for agreement with the photometric rotational period. Wolf 1069 is an $H\alpha$ -inactive star ($pEW'(H\alpha) \text{ \AA} > -0.3$; Schöfer et al. 2019).

While there are no strong or moderate correlations found between the RVs and the stellar activity indicators using the Pearson’s p -probability, the GLS periodograms of the indicators nonetheless consist of a variety of prominent peaks (see

Fig. 4). While some peaks found in the periodograms do coincide with the rotation period derived from the photometry, that is, ~ 169 d, there are nonetheless other existing signals with even higher significance ranging in periods from ~ 200 – 260 d, or even in the longer-period regime of up to a few hundred days. Particularly, these signals are present in the CRX, dLW, $H\alpha$ index, TiO λ 7050 \AA , TiO λ 8430 \AA , TiO λ 8860 \AA , CTR,

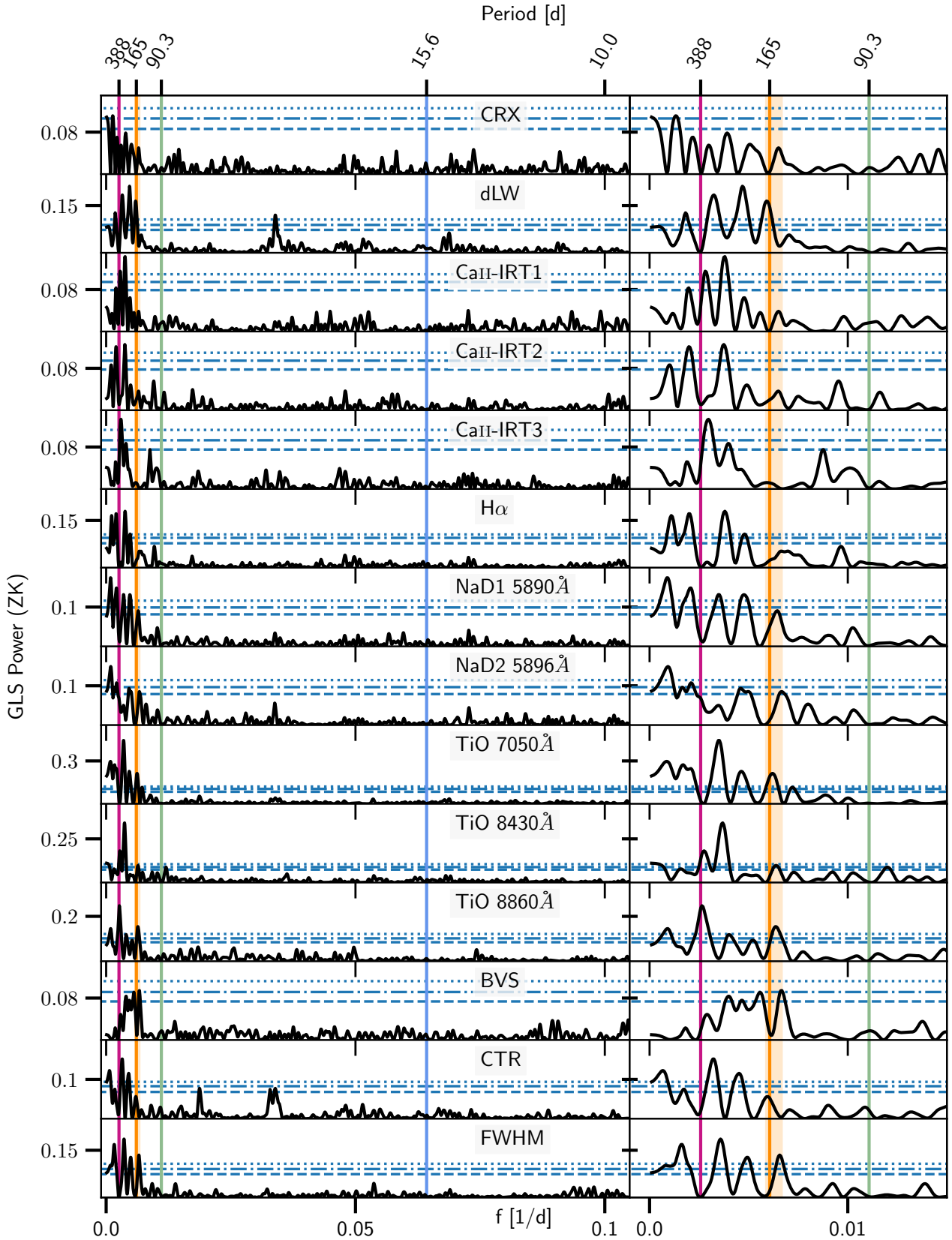


Fig. 4. GLS periodograms for various known stellar activity indicators from the CARMENES spectroscopy. The window function of the data sampling can be found in Fig. 5a. For consistency, the colored vertical lines and the frequency width of the panels on the left correspond exactly to those in the RV GLS periodograms (Fig. 5). The horizontal dashed, dot-dashed, and dotted blue lines represent the 10, 1, and 0.1% FAP levels (from bottom to top).

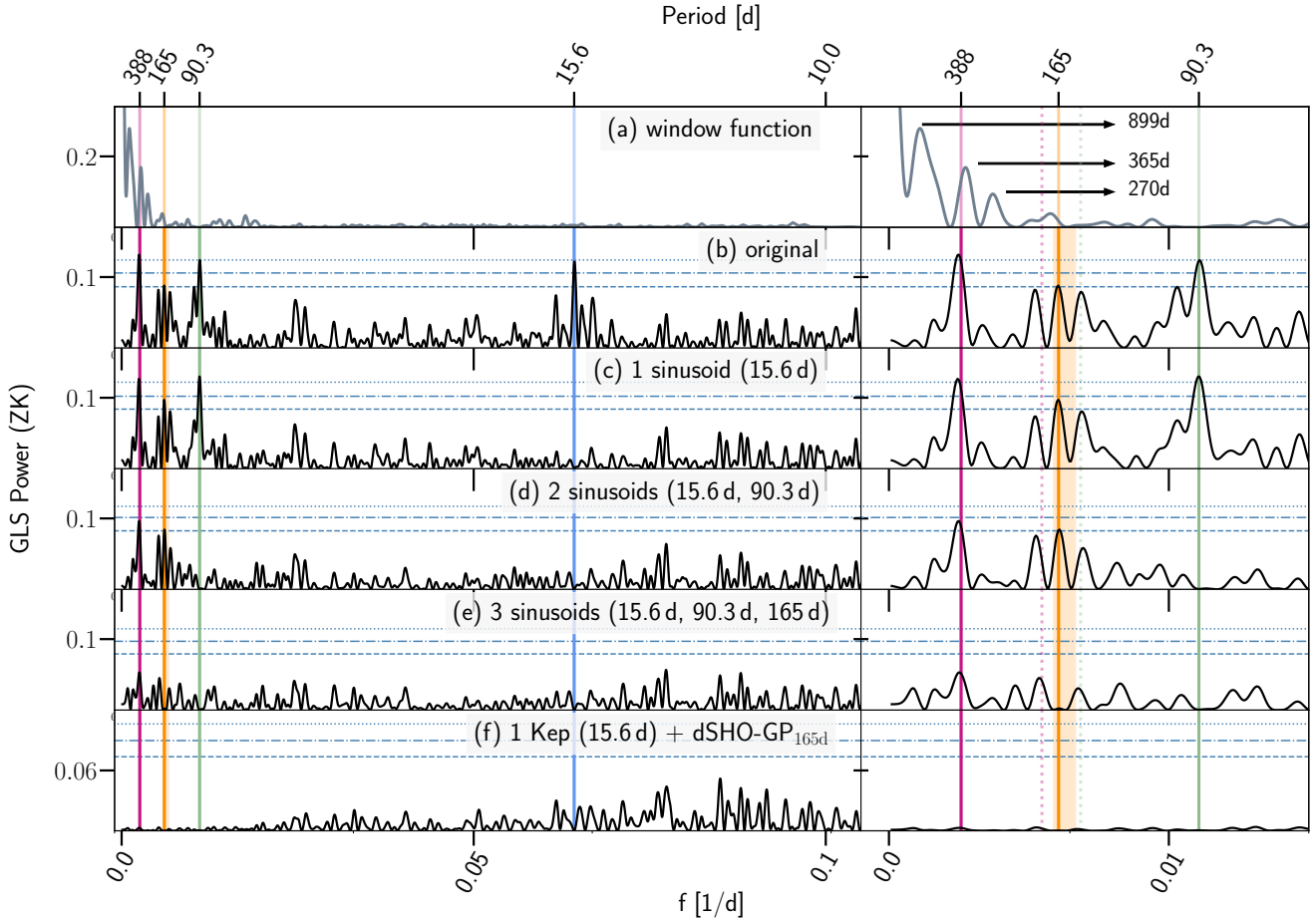


Fig. 5. GLS periodograms for the RVs of Wolf 1069 after sequentially subtracting out the most prominent signals. The horizontal dashed, dot-dashed, and dotted lines represent the 10, 1, and 0.1% FAP levels (from bottom to top). There were no significant signals with periods shorter than 10 d other than the aliases due to the daily sampling. The right panel is a closer zoom-in of the left panel to highlight the longer-period signals. The 15.6 d planetary signal is illustrated with a vertical blue solid line, and the 90.3 d signal and its alias due to the 270-d sampling with a green solid and dashed line, respectively. The range for the photometric rotation period is shaded in orange, where the stellar rotation period within the RVs is marked with an orange solid line. The component of residual telluric contamination at 388 d and its alias due to the 365-d sampling period are also represented with a vertical magenta solid and dashed line, respectively. Panel a: the window function of the data set. Panel b: no signal fitted, solely the original RVs with an offset and jitter term. Panel c: residuals after subtracting the 15.6 d signal. Panel d: residuals after subtracting a simultaneous model fit of two sinusoids at 15.6 and 90.3 d. Panel e: residuals after subtracting a simultaneous model fit of three sinusoids at 15.6, 90.3, and 165 d. Panel f: residuals after subtracting the final model choice including 1 Keplerian at 15.6 d (further described in Sect. 4.2).

and FWHM. There are still instances where the significant peaks coincide with the expected alias frequencies, however, the power at the rotational period is sometimes consistent with zero, as for instance in the Ca II IRT3 indicator. This could be pure coincidental, we cannot exclude the possibility of it being a chance alignment. There are also peaks at even longer-period regimes (i.e., >1000 d), which could be due to a stellar magnetic cycle not related to the stellar rotation itself. This behavior appears similar to EV Lac (see Jeffers et al. 2022, for a detailed analysis of the various periodicities), where it was shown that different indicators can respond with a phase lag, or nonuniformly with the rotational variation of the star. In this work, we focus only on signals pertaining to the stellar rotation period, as well as those connected to the other RV signals (see Sect. 4.1).

Wolf 1069 is considered to be a low-activity, low-mass star following the categorizations in Lafarga et al. (2021). Hence, applying the findings made by Lafarga et al. (2021), the most effective indicators for identifying the stellar rotation period comprise the dLW, CTR, and FWHM, which are tracing the varying width of the absorption lines in the spectra, as well as the indices of the chromospheric lines, $H\alpha$ and Ca II IRT,

and sometimes the RVs themselves. The CRX and BVS in this instance are not as beneficial. Taking a closer look at these, we see that in fact, the dLW does peak at the expected rotation period and fits quite well to it. Likewise, when fitting for 169 d, the CTR and FWHM also match quite well in the phase-folded plots (not shown). The $H\alpha$ index and Ca II IRT, however, do not agree with this periodicity, but rather show long-term trends, that may be related to a longer magnetic cycle as these indicators are also associated with magnetic cycles. Another significant signal to mention in the dLW and the CTR appears at ~ 29.5 d, which is close to twice the orbital period of the planetary signal of interest (i.e., 15.6 d, see Sect. 4.2). However, this periodicity is most likely due to instrumental effects, namely, the contamination from the light of the Moon. Within the RVs, there is a peak at 165 d, though not significant, after subtracting out the other more prominent peaks (see Fig. 5d). When performing the final fit on the RVs (see Sect. 4.2), we apply a dSHO-GP on this signal arriving at a value of $P_{\text{rot, RV}} = 165.6^{+3.3}_{-3.4}$ d.

To bring all this evidence together, the photometric data point to a rotational period of ~ 169 d, the RVs to ~ 165 d, and a portion of stellar activity indicators similarly hint toward this

Table 3. Aliases of the significant peaks found in the RVs given the sampling period tabulated.

Sampling periods (d)	Alias order	Present periods (d)			
		15.6 ($f = 0.06410 \text{ d}^{-1}$)	90.3 ($f = 0.01107 \text{ d}^{-1}$)	165 ($f = 0.00602 \text{ d}^{-1}$)	388 ($f = 0.00258 \text{ d}^{-1}$)
270 ($f_s = 0.00370 \text{ d}^{-1}$)	$m = 1$	14.8 [†]	67.7 [†]	102.8	159.2*
	$m = -1$	16.6	135.7	431.0*	887.8
	$m = 2$	14.0 [†]	54.1 [†]	74.5	100.2
	$m = -2$	17.6	272.7	722.9	207.0
365 ($f_s = 0.00274 \text{ d}^{-1}$)	$m = 1$	15.0	72.4 [†]	114.1 [†]	188.1
	$m = -1$	16.3	120.0	304.5 [†]	6157.4
	$m = 2$	14.4 ^{†*}	60.4*	86.9	124.1
	$m = -2$	17.1	178.7	1836.1	344.6
899 ($f_s = 0.00111 \text{ d}^{-1}$)	$m = 1$	15.3 [†]	82.1 [†]	140.1	271.0
	$m = -1$	15.9 [†]	100.4	203.6	682.6
	$m = 2$	15.1	75.2 ^{†*}	121.2	208.3
	$m = -2$	16.2	113.0	263.2	2835.9

Notes. The periods of the aliases are computed using $P_{\text{alias}} = 1/f_{\text{alias}}$, where $f_{\text{alias}} = f + m \cdot f_s$ following f as the frequency of the true signal, m as the alias order, and f_s as the sampling frequency. Aliases that are significant (FAP > 10%) are bolded, whereas those that are present but not significant are indicated with a dagger †. Ones marked with an asterisk signify peaks that are close to, but not exactly, the center of the expected alias.

value, though sometimes exhibit higher peaks at longer periods. Based on the photometry, it is evident that the variability of the star is changing from season to season (see Fig. 2), so the periodicities detected in the indices skewing away from the predicted rotational period may be exhibiting the evolution of the spot configuration. For example, some activity indices are evidently still consistent (i.e., same period or aliasing due to the sampling), although others are not as consistent, which could be a result of other issues, stellar cycles, spot evolution, data precision and sampling, that make the interpretation nontrivial. We therefore adopt the rotational period of Wolf 1069 to be within the range of 150–170 d, with indications toward $P_{\text{rot}} = 169.3^{+3.7}_{-3.6}$ d, though values outside this constrained range cannot be easily excluded. This is consistent with the predictions for a low-mass, inactive M dwarf (Newton et al. 2017, their Fig. 5).

4. Analysis and results

4.1. Signal detection

We first computed a GLS periodogram on the RVs using the Exo-Striker¹⁵ tool (Trifonov 2019) to initially identify potentially interesting signals. A series of GLS periodograms after sequentially subtracting out the most prominent sinusoidal signals, along with the discrete Fourier transform of the window function, can be found in Fig. 5. The sampling of the data showed three notable peaks at 899 d, 365 d (the yearly sampling), and 270 d. To quantify the significance of a signal's peak, we computed the false alarm probability (FAP) levels of 10, 1, and 0.1% using 10 000 randomizations of the input data where the frequency ranged from $1/t_{\text{baseline}}$ to 1, with a frequency resolution of $1/t_{\text{baseline}}$ and oversampling factor of ten.

Already, in the original RV data set there are three prominent peaks at 15.6 d, ~90–100 d and ~400 d, all hovering the 0.1% FAP level (Fig. 5 b). To also mention, there are equally prominent peaks at 0.94 d and 1.066 d, both aliases of the 15.6 d signal

due to the daily sampling. Furthermore, there are strong yearly aliases for the 15.6 d signal, particularly at 14.9 d and 16.2 d. Performing tests with the AliasFinder (Stock & Kemmer 2020), we find that the true periodicity is the one at 15.6 d (see Fig. A.1), which we adopt when considering this signal. Continuing on, there are an additional three peaks around the 10% FAP level, namely at 165 d, ~190 d, and ~145 d, in order of significance, where the first one corresponding to the rotation period. The other two can be explained as aliases due to the 365-d and 270-d sampling of the ~400 d and ~90–100 d signal, respectively. A full outline of all the aliases is tabulated in Table 3.

As it does not matter which of the peaks of equal significance is chosen first to subtract out for the prewhitening, we opt for the 15.6 d considering its aliases are also those that are most prominent. After subtracting the 15.6 d signal (Fig. 5 c), all corresponding aliases disappear, as expected. Both the ~90–100 d and ~400 d signal reach above the 0.1% FAP level, where the 165 d, ~190 d, and ~145 d signals also become more prominent. In the next succession of simultaneously modeling a two-sinusoidal model with the next highest peak (15.6 d, 90.3 d), there are no longer any signals that have an FAP level less than 0.1%. The highest peak at ~400 d is above the 10% FAP level, and its alias due to the yearly sampling (i.e., ~190 d) is apparent but no longer significant. The 165 d is still above 10% FAP level.

The next signal to subtract for would be the one at ~400 d. However, we have evidence that this signal is related to telluric contamination. We specifically compared the nontelluric-corrected RVs with those corrected for tellurics, finding that there is a prominent peak at 388 d in the telluric component (Fig. 6, top panel). We conclude that even though we use the telluric-corrected spectra, the contamination still likely manifests as this process of telluric removal is nontrivial and, nonetheless, introduces residuals in the corrected spectra (Nagel et al. 2022). Moreover, the peak in the RVs is more so at 404 d, whereas the peak in the periodogram of the telluric component is actually at 388 d. We presume that this could be due to the fact that the alias due to the 270-d sampling of the 165 d signal is 420 d, thus, adding some power there, in turn broadening

¹⁵ <https://github.com/3fon3fonov/exostriker>

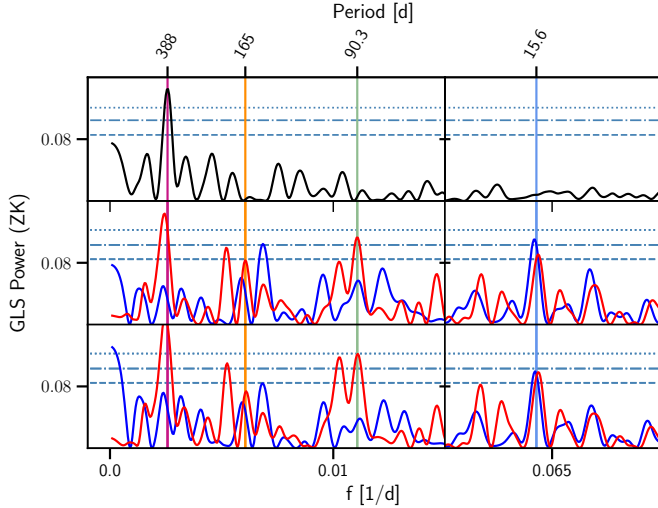


Fig. 6. GLS periodograms of the telluric-only (nonTC subtracted from TC; top), nonTC (middle) and TC (bottom) RVs. The red and blue colors represent the “blue” and “red” subsets within the VIS channel of the CARMENES instrument (Sect. 4.3). The vertical lines match those in Fig. 5 for consistency and the horizontal lines are identical in the bottom panels but differ slightly from the top panel.

the peak and veering the periodicity away from 388 d to a value in between the two. With this in mind, and considering the photometrically determined rotation period, we proceed with simultaneously subtracting the 165 d signal next. Finally, there are no more signals above 10% FAP after removing three simultaneous sinusoidal signals (15.6 d, 90.3 d, 165 d).

4.2. RV model comparison

Out of the three prominent signals, only the one at 165 d does not reach our significance criterium (FAP < 0.1%, though greater than 10%), but is however related to stellar activity and thus might be important to model. We therefore continue the analysis by testing out “three-signal models” while properly considering the activity, with comparison to “two-signal models” by ignoring it. For reasons explained in Sect. 4.3, the origin of the 90.3 d is ambiguous. Thus, we model it solely with a sinusoid when including this signal in a fit. For the 15.6 d signal, there is no evidence against it to not be planetary, therefore, we apply circular or eccentric Keplerian orbits. For eccentric fits, the eccentricity was parametrized with $S_1 = \sqrt{e} \sin \omega$ and $S_2 = \sqrt{e} \cos \omega$ with uniform priors, $\mathcal{U}(-1, 1)$ as recommended by Eastman et al. (2013).

The modeling and comparison of models is all performed with `juliet`, a versatile python package for simultaneous transit and RV fitting, as already described in depth in other works such as Kemmer et al. (2020), Stock et al. (2020), Bluhm et al. (2020), and Kossakowski et al. (2021). Following the same recipe as in the mentioned references, we use the computation of the Bayesian log evidence ($\ln \mathcal{Z}$) to compare models. Models with a $\Delta \ln \mathcal{Z} \geq 2.5$ in comparison to another one show moderate evidence in favor of the winning model (e.g., Trotta 2008; Feroz et al. 2011). Any value greater than 5 signifies strong evidence toward the winning model and anything below 2.5 indicates that neither of the two models are favored.

To begin, we first ran a flat model with a white-noise term (i.e., jitter term, $\sigma_{\text{CARMENES-VIS}}$) to act as a basis. Likewise, we ran a red-noise model using a dSHO-GP centered around

Table 4. Model comparison using the Bayesian log evidences on the RVs for Wolf 1069.

Model	$\ln \mathcal{Z}$	$\Delta \ln \mathcal{Z}$
<i>Base models</i>		
Flat	-640.00	-33.14
dSHO-GP _{165 d}	-618.51	-11.65
<i>One-signal model</i>		
1 Kep _{15.6 d}	-631.49	-24.63
<i>Two-signal models</i>		
1 Kep _{15.6 d} + 1 Sin _{90.3 d}	-620.62	-13.76
1 Kep_{15.6 d} + dSHO-GP_{165 d}	-606.86	0.0
<i>Three-signal models</i>		
1 Kep _{15.6 d} + 2 Sin _{90.3 d, 165 d}	-616.83	-9.96
1 Kep _{15.6 d} + 1 Sin _{90.3 d} + dSHO-GP _{165 d}	-606.94	-0.08

Notes. The chosen model was the 1 Kep_{15.6 d} + dSHO-GP_{165 d}, as marked as the bold-faced row. A better model would have a larger, more positive $\Delta \ln \mathcal{Z}$. Regarding the model names, “Kep” refers to a circular Keplerian orbit and “Sin” to a sinusoidal signal. The period values are quoted as the median of the posterior distribution and can vary slightly depending on the model choice.

the stellar rotation period (see below for setup details). For the 15.6 d signal, we imposed an appropriately sized uniform prior for the period, $\mathcal{U}(15.4 \text{ d}, 15.7 \text{ d})$ in order to cover the width of the peak as in the periodogram and to ensure that this true signal would be picked up rather than its nearby aliases. The time-of-transit center, which is used in `juliet` to parametrize the phase of the orbit, was chosen to be uniform and set to cover one cycle during the most-sampled time epoch of the RV data set, $\mathcal{U}(2458502 \text{ d}, 2458515 \text{ d})$. Likewise, for the $\sim 90 \text{ d}$ signal, the prior on the period was kept wide enough to capture the tails of the posterior sample distribution, $\mathcal{U}(85 \text{ d}, 95 \text{ d})$. To account for the stellar rotation period, we experimented modeling it with a sinusoid and with a dSHO-GP. The photometrically determined rotational period of 150–170 d (Sect. 3.2) was taken into consideration for the prior setup on the period. Within the RV periodograms (Sect. 4.1), the periodicity shows up as closer to 165 d and encounters various neighboring signals due to aliasing of the other signals. For this reason, the prior on the period was kept relatively narrow and uniform from 155 d to 175 d. Table C.2 showcases a full overview of the employed priors, including those for the instrument.

Results. A table showcasing the Bayesian log evidence for the assortment of the tested models tested can be found in Table 4. The winning model comprises one Keplerian for the 15.6 d signal alongside a dSHO-GP centered on 165 d to describe the behavior of the stellar rotation period. We note that including an extra sinusoid term for the 90.3 d signal to this model is equivalent in terms of the Bayesian log evidence, even though this signal is evidently prominent in the GLS periodogram (Fig. 5). Given the ambiguity of the nature of this signal (Sect. 4.3), we find it appropriate to omit it from the final model and allow the dSHO-GP to moderately absorb it for the time being. The crucial aspect is that the interpretation of this signal and, thus, how we consider it in our models, which we acknowledge may adjust in the future, does not drastically alter the planetary parameters of the 15.6 d signal (Fig. 7).

For the 15.6 d signal, an eccentric Keplerian orbit was consistent with a circular one. The distribution of the eccentricity

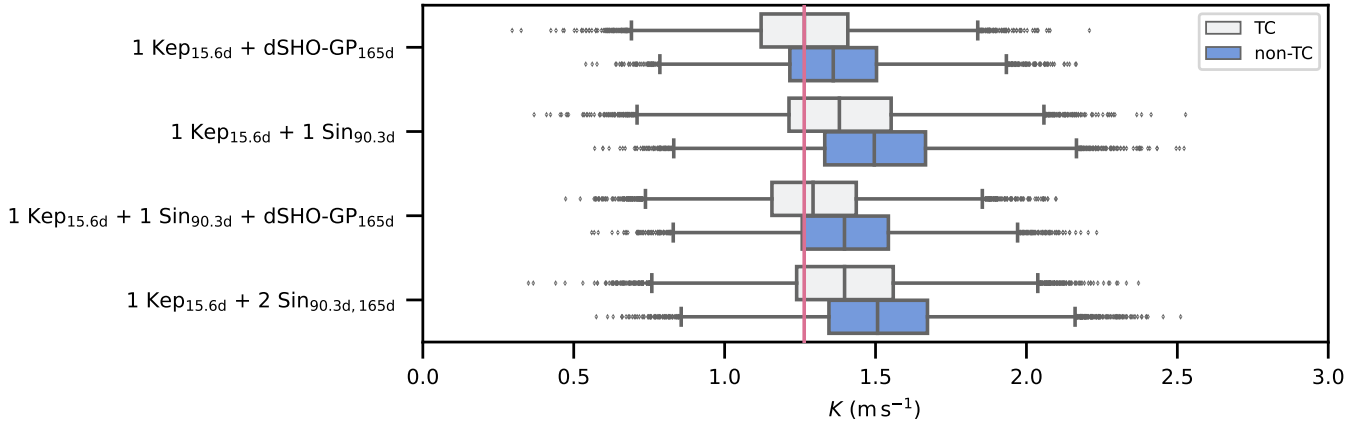


Fig. 7. Box plot of the posteriors for the distributions of the minimum mass for the 15.6 d signal based on the model choice. The gray and blue boxes represent the 25 and 75% quartiles of the posterior from the telluric-corrected (TC) and nontelluric-corrected (nonTC) RVs, respectively. The red vertical line represents the median value of the minimum mass of the 15.6 d signal when applying the most favored model. The extending gray lines depict the rest of the distribution and the dots are deemed as “outliers”. The models named here match those in Table 4.

Table 5. Derived posterior parameters for Wolf 1069 b.

Parameter name	Posterior ^(a) b	Unit
P_p	$15.564^{+0.015}_{-0.015}$	d
$t_{0,p}$ (BJD)	$2458511.63^{+0.45}_{-0.46}$	d
K_p	$1.07^{+0.17}_{-0.17}$	m s^{-1}
$S_{1,p} = \sqrt{e_p} \sin \omega_p$	0.0 (fixed)	...
$S_{2,p} = \sqrt{e_p} \cos \omega_p$	0.0 (fixed)	...
$M \sin i_p$	$1.26^{+0.21}_{-0.21}$	M_\oplus
a_p	$0.0672^{+0.0014}_{-0.0014}$	au
$T_{\text{eq}}^{(b)}$	$250.1^{+6.6}_{-6.5}$	K
S_p	$0.652^{+0.029}_{-0.027}$	S_\oplus

Notes. ^(a)Error bars denote the 68% posterior credibility intervals. ^(b)The equilibrium temperature of the planet assuming zero Bond Albedo and one emissivity.

was consistent with zero. Focusing on the stellar rotation period, the dSHO-GP was preferred over a sinusoid ($\Delta \ln \mathcal{Z} > 10$) as it is most likely better suited in describing the quasi-periodic behavior of the stellar activity. Furthermore, this corresponds well to the fact that there seems to be a high level of spot evolution as we have encountered in the stellar activity indicators (Sect. 3.2) such that this is also demonstrated as an effect in the RVs.

To conclude, the final model consists of ten free parameters applied on the 262 RV data points. The 15.6 d signal is best described by a circular Keplerian model and the 165 d signal by a dSHO-GP to account for the stellar rotation period. The best RV model from the posteriors is shown in Fig. 1, where values for the derived planetary parameters can be found in Table 5. The full posterior overview for all model parameters is located in Table C.3. A visual inspection of the posterior probability densities for key parameters are displayed in Figs. C.1 and C.2.

4.3. Investigating the low-amplitude 90.3 d signal

The 90.3 d signal is significant with an FAP level near 0.1% in the GLS periodograms (Fig. 5), yet it does not statistically

improve the fit when including it in the RV models including also the rotation period (Table 4). This could be an artifact that the semi-amplitude hovers around the 1 m s^{-1} limit ($K_{90.3 \text{ d}} = 91 \pm 38 \text{ cm s}^{-1}$), thus, making it possibly difficult to justify including such a low-amplitude signal with a relatively large uncertainty in the models. Likewise, the dSHO-GP kernel used in the model is equipped to pick up the rotational period, P_{rot} , and half of the rotational period, $P_{\text{rot}}/2$. It could be that 90.3 d is decently close to 83 d (i.e., $P_{\text{rot}}/2$) and, thus, the dSHO-GP is performing its job of absorbing this signal. In fact, this is demonstrated in the GP component of the RV model shown in Fig. 1. It is nonetheless evident that this periodicity is present in the RV data as can be seen in the residuals of the RV model. Its nature, however, appears to be quite dubious. Below, we explore the signal further to better understand its origin.

Its periodicity is near a quarter of one year. A suspicion could be that this signal should be present in the telluric-contamination-only component of the RVs, though, it is not (Fig. 6, top panel). We additionally tested breaking up both the telluric-corrected (TC) and nontelluric-corrected (nonTC) RVs into “blue” and “red” subsets. To do this, we can recompute the RVs by selecting certain orders. The CARMENES VIS channel consists of 55 RV orders, 42 of which are used to compute the RV measurement via a weighted mean through *serval* (Zechmeister et al. 2018). For the blue and red subset, we considered the first 21 and last 21 orders, respectively. Thus, the blue and red subsets span roughly 570–700 nm and 700–910 nm, respectively. A GLS periodogram for both subsets and for both data sets is shown in Fig. 6. Taking a look at the nonTC spectra, the 388 d (telluric-attributed) signal, its yearly alias at 188 d, and the 90.3 d, as well as a neighboring signal at 97 d, are substantially stronger in the red than in the blue. This is in agreement that the telluric contamination is stronger in the red than in the blue, given that there are sharper, deeper telluric-absorption features in the redder part of the VIS channel (Fig. 1 in Reiners et al. 2018). Meanwhile, the power of the 15.6 d and 165 d signals is consistent within one another in both subsets. After the telluric correction, some residual telluric contamination remains, though dampened, indicating that the correction for tellurics was indeed effective but left some residual effect as can be seen in the RV periodograms (Fig. 5). The power of the 15.6 d and 165 d signals is still compatible, which is most important. Therefore, even though the 90.3 d has no appearance

in the telluric-contamination-only component, it does exhibit chromaticity and behavior similar to other telluric signals, pointing less in favor of a planetary signal and potentially more in favor of telluric effects. It is, however, puzzling as to why the 90.3 d signal does not peak in the telluric-only RVs (Fig. 6).

To summarize, we are not able to distinctly decipher the origin of the 90.3 d signal. Even if it were planetary, we currently do not have enough evidence to support this claim. As our main concern is the 15.6 d signal and we presented that its planetary parameters are independent of whether the 90.3 d signal is considered or not (Fig. 7, particularly between 1 $\text{Kep}_{15.6\text{d}} + 1 \text{dSHO-GP}_{165\text{d}}$ and 1 $\text{Kep}_{15.6\text{d}} + 1 \text{Sin}_{90.3\text{d}} + \text{dSHO-GP}_{165\text{d}}$), we choose not to include this signal in the final model as a precaution. Further investigation or RV monitoring may be beneficial, however, this lies beyond the scope of this paper.

4.4. Transit search within TESS

With a minimum mass of $1.26 \pm 0.21 M_{\oplus}$ and assuming an Earth-like core-mass fraction of 0.26, we obtained a radius estimate of $1.08 R_{\oplus}$ for Wolf 1069 b using the mass-radius relation as given by Zeng et al. (2016). This then translates to an expected transit depth of ~ 3.6 ppt, which should be easily detectable with TESS, though not with the other available photometric facilities (i.e., SuperWASP and MEarth). The transit probability is however rather low at 1.2% ($p \approx R_{\star}/a_p$). Nonetheless, propagating the orbital period and t_0 from the RV fit with their $1-\sigma$ uncertainties (taken from Table 5), we unfortunately did not find any hint of a possible transit. We additionally checked to confirm that the transits could not have happened during the data gaps, where only one would fall within an observational gap. Likewise, we checked with the transit-least-squares¹⁶ method (Hippke & Heller 2019), though no interesting signals popped up. Given this information, we were able to obtain a maximum inclination for Wolf 1069 b of $i_{\text{max}} = \arccos(R_{\star}/a_p) = 89.35$ deg.

5. Discussion

5.1. On the promising habitability of Wolf 1069 b

Plugging in the stellar luminosity and effective temperature (Table 2), Wolf 1069 b, with a distance of 0.0672 ± 0.0014 au to the star, sits comfortably within the conservative HZ limits, namely, 0.056–0.111 au given the runaway-greenhouse and maximum-greenhouse limits, respectively (Kopparapu et al. 2013, 2014). Even more so, it is very likely that Wolf 1069 b is indeed an Earth-like planet with Earth-like composition (32.5% iron mass fraction and 67.5% silicates) and radius around one Earth radii (following Fig. 1 in Luque & Pallé 2022), as we also estimated in Sect. 4.4. Figure 8 puts Wolf 1069 b in context with other planets around M-dwarf stars that are most likely to have a rocky composition and maintain surface liquid water as listed in the Habitable Exoplanet Catalog¹⁷ with some modifications (Appendix B). To this effect, Wolf 1069 b resembles best Proxima Centauri b, GJ 1061 d, Teegarden’s Star c, Kepler-1649 c, and GJ 1002 b and c. With the exception of Kepler-1649 c, all are RV-only detections. Furthermore, all 14 planetary systems illustrated contain more than one planetary companion, excluding Wolf 1069, Ross 128, and Kepler-1229, as discussed in Sect. 5.2. When considering the occurrence rate for planets with 1–10 Earth masses on periods shorter than 10 d around later-type

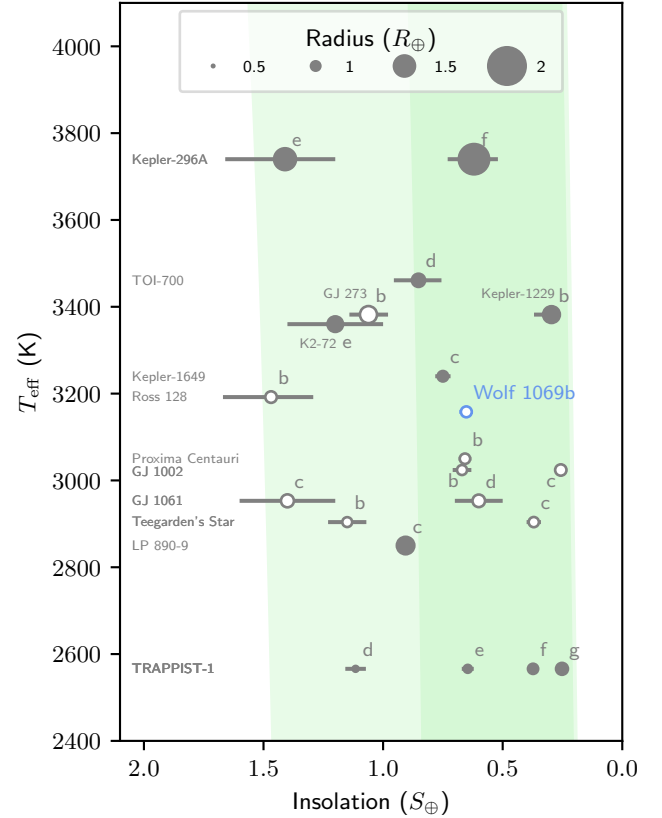


Fig. 8. M-dwarf ($T_{\text{eff}} < 4000$ K) planetary systems with at least one detected planet in the conservative sample of potentially habitable exoplanets (i.e., $0.5 R_{\oplus} < R_p < 1.6 R_{\oplus}$ or $0.1 M_{\oplus} < M \sin i_p < 3 M_{\oplus}$) defined by the Habitable Exoplanet Catalog. The optimistic and conservative HZ regions for a one Earth-mass planet following the definition as set out by Kopparapu et al. (2013) are shaded with light and dark green, respectively. Only the planets in either the conservative or optimistic HZ of each planetary system are shown. White-filled and gray-filled points indicate nontransiting and transiting detections, respectively. The size of the circles is proportional to the planetary radius, estimated with the mass-radius relationship of Zeng et al. (2016) for nontransiting RV planets. The data used in this plot is further discussed in Appendix B. Plot inspired by Zechmeister et al. (2019) and Dreizler et al. (2020).

M dwarfs, this value lies between ~ 0.56 – 1.75 planets per star (Ribas et al. 2023; Hardegree-Ullman et al. 2019). Regarding the proximity of these systems, Dressing & Charbonneau (2015) estimated that the nearest nontransiting HZ planet could be 2.6 ± 0.4 pc away, and is within 3.5 pc with 95% confidence for potentially habitable 1– $1.5 R_{\oplus}$ planets. Soon after, Proxima Centauri b was discovered at a distance of 1.30 pc (Anglada-Escudé et al. 2016), GJ 1061 d at 3.67 pc (Dreizler et al. 2020), Teegarden’s Star c at 3.83 pc (Zechmeister et al. 2019), and GJ 1002 b and c at 4.85 pc (Suárez Mascareño et al. 2023). Wolf 1069 b is located at a distance of 9.57 pc, making it the sixth closest, conservative HZ Earth-mass planet to us. Other closer contenders included Ross 128 b ($d = 3.38$ pc) and GJ 273 b ($d = 5.83$ pc), though these planets lie in the optimistic HZ.

Wolf 1069 b is in the slow rotator regime, and possibly in tidal equilibrium rotation (e.g., Heller et al. 2011), that can lead to unique atmospheric circulation pathways (e.g., Dole 1964; Yang et al. 2019; Del Genio et al. 2019b). The impacts of this slow rotation on both the potential habitability and impact on observations have been discussed in detail by several 3D GCMs (see e.g., Edson et al. 2012; Leconte et al. 2013). Preliminary

¹⁶ <https://github.com/hippke/tls>

¹⁷ <https://personal.ems.psu.edu/~ruk15/planets/>

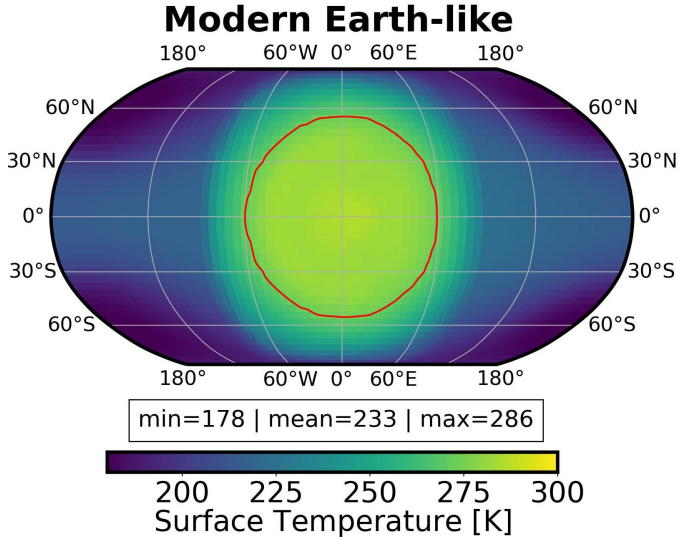


Fig. 9. Surface temperature map of Wolf 1069 b produced by the ExoCAM GCM, assuming a Modern Earth-like atmosphere. The map is centered at the substellar point and the red line delimits the area where water is at the liquid phase on the surface.

results from GCMs climate simulations using both the ExoCAM model (Wolf et al. 2022) and the ROCKE-3D model (Way et al. 2017) suggest that Wolf 1069 b could maintain moderate temperatures and surface liquid water for a large range of atmospheric compositions and surface types. Simulations explore a variety of surface pressures, N_2 , CO_2 , CH_4 , and H_2O abundances, along with desert, solid rock, slab ocean, and dynamic ocean surfaces. The comprehensive analysis of these 3D climate results and the observational signals that could be used to differentiate between climate states of Wolf 1069 b show the planet to be durably habitable (Crouse et al., in prep.). Figure 9 shows the surface temperature map produced with the ExoCAM GCM assuming a Modern Earth-like atmospheric composition. The red line delimiting the open ocean shows that a significant fraction of the day side surface could maintain liquid water, therefore day-side habitable conditions. While the presence and nature of any atmosphere on Wolf 1069 b (and existing M-dwarf planets in general) remains theoretical, the support of habitable conditions over such a wide range of possible atmospheric states puts Wolf 1069 b in the same elevated class as Proxima Centauri b (Turbet et al. 2016; Del Genio et al. 2019a), TRAPPIST-1 e (Wolf 2017; Turbet et al. 2018; Fauchez et al. 2019), and TOI-700 d (Suissa et al. 2020) as a primary target to search for habitability and biosignature markers.

Similar to Proxima Centauri b, Wolf 1069 b does not transit its host star, meaning that observation and analysis of thermal emission and reflected light phase curves will need to be employed to probe its atmosphere. Given the brightness of the host star and the distance to Earth, and assuming atmosphere models and albedo similar to the ones predicted for the TRAPPIST-1 planets and Proxima Centauri b (Turbet et al. 2022), the atmospheric characterization of Wolf 1069 b might be within the reach of the ELT¹⁸ instrumentation. ANDES¹⁹ (formerly known as HIRES; Maiolino et al. 2013) will be the first instrument theoretically capable of detecting the reflected light from HZ rocky planet atmosphere in the early 2030's. However,

¹⁸ Extremely Large Telescope.

¹⁹ ArmazoNes high Dispersion Echelle Spectrograph, <https://elt.eso.org/instrument/ANDES/>

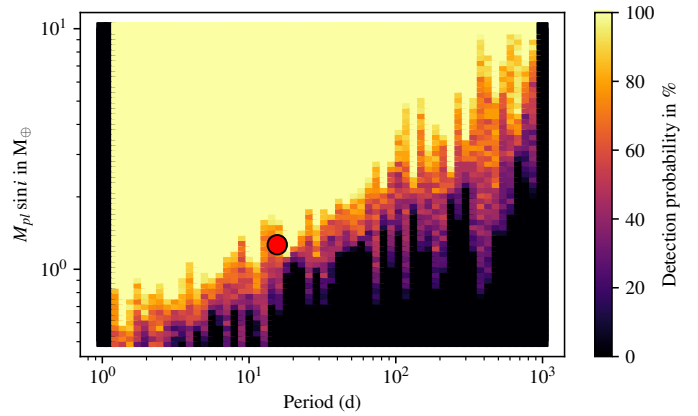


Fig. 10. RV detection map of Wolf 1069 from an injection-and-retrieval experiment after subtracting the 15.6 d, 90.3 d and 165 d signals. The red circle indicates the planet Wolf 1069 b.

for Wolf 1069 b, the small angular separation in the sky between the planet and the host stars, 7.01 milliarcsec, makes these observations very challenging, even with the use of extreme adaptive optics systems. Further instrumental advances, such as the proposed PCS²⁰ instrument for the ELT (Kasper et al. 2021) or space-based coronagraphic/interferometric missions, might be needed. While such observations are very challenging, many of the nearest planets found in the conservative HZ around M dwarfs are nontransiting, RV detections, indicating that perhaps more time and investment into the development of such observations should be considered if we want to establish ground statistics using all of the thus-far detected, potentially habitable worlds.

5.2. The case of Wolf 1069 b as a lone, short-period planet

Our comprehensive analysis of the RV and photometric data suggests that Wolf 1069 b is the only bonafide planet in the sensitive domain of the planetary parameter space. We characterized this domain with injection-and-retrieval tests by taking the residuals of the winning model without a GP (Sect. 4.2) and creating simulated RV time series using Eq. (2) in Sabotta et al. (2021). This was repeated 50 times on 30 log-uniformly distributed grid points in mass and 60 in period, allowing us to rule out additional planets with at least one Earth mass and periods of less than 10 days (Fig. 10). Wolf 1069 b joins a sample of currently two RV-detected, single terrestrial planets ($\lesssim 2 M_\oplus$), which have all been detected around M dwarfs less massive than $0.5 M_\odot$. These objects are GJ 393 b (Amado et al. 2021) and Ross 128 b (Bonfils et al. 2018), where the former resides in the HZ region of its host star (see also Sect. 5.1), whereas the latter receives too much flux. Likewise, transiting planets following the same criteria include GJ 367 b (Lam et al. 2021) and GJ 1252 b (Shporer et al. 2020), where the latter has rather a tentative measured mass of $2.09 \pm 0.56 M_\oplus$ and both are not found in the HZ of their parent stars. Nonetheless, the small sample size raises the question how frequent the solitary occurrence of such a planet is. The overall occurrence rate of small, rocky planets on close orbits has been shown to be larger around host stars of later spectral type (e.g., Mulders et al. 2015; Hardegree-Ullman et al. 2019; Hsu et al. 2020). However, there is some indication that this rule might not apply for the latest M dwarfs (Gibbs et al. 2020; Sebastian et al. 2021;

²⁰ Planetary Camera and Spectrograph.

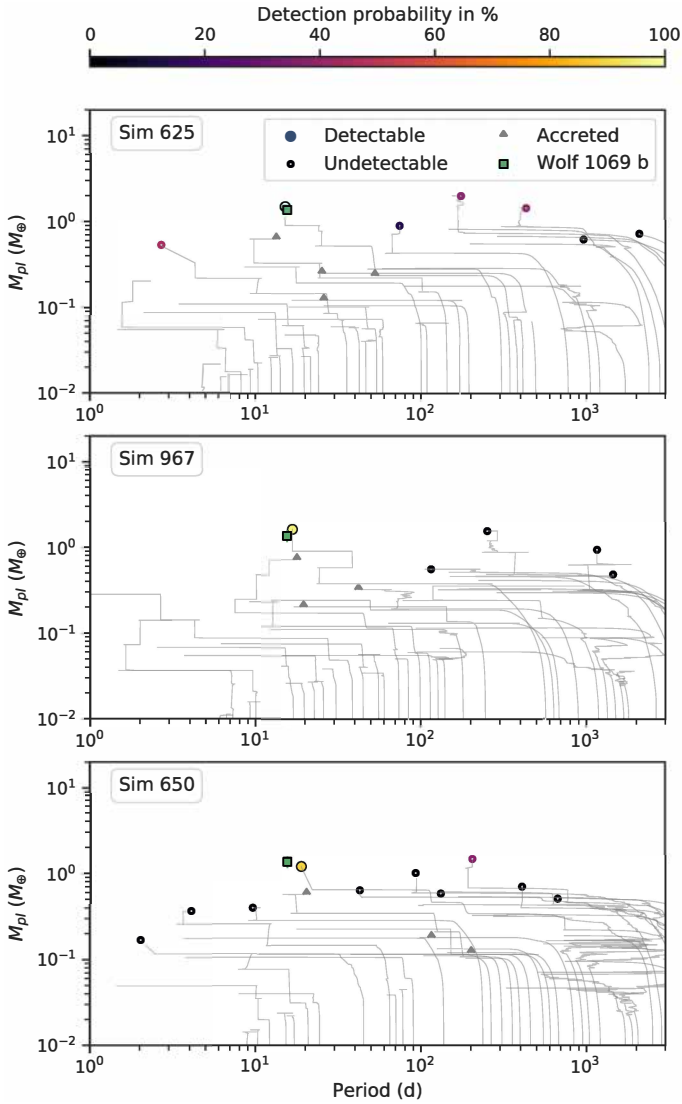


Fig. 11. Formation paths and final planets in planet formation simulations taken from the population synthesis work of [Burn et al. \(2021\)](#). We show the three simulations with a single detectable planet closest to Wolf 1069 b in relative mass and orbital period. A planet is labeled “undetectable” if the detection probability is below 50%. Formation tracks are shown as gray lines that can end in either a filled circles (detectable planet), a triangle (accreted by detectable), a ring (undetectable), or without a marker (accreted by other planets or ejected).

[Sestovic & Demory 2020](#); [Brady & Bean 2022](#); [Mulders et al. 2021](#)) and that systems, such as the one presented here, could be in fact rare.

Planet formation models following the core accretion paradigm ([Pollack et al. 1996](#)) generally suggest a high multiplicity of Earth-mass planets around mid-M-dwarf host stars ([Burn et al. 2021](#)). However, these models produce many planets beyond current detection limits, and bias-corrected synthetic populations show sufficiently reduced rates to be compatible with the observations ([Schlecker et al. 2022](#)). The discovery of a single planet comparable to Wolf 1069 b is consistent with this picture.

We tested this scenario by applying the computed detection sensitivity (Fig. 10) to the synthetic planetary population *NGM10* around an $0.1 M_{\odot}$ star presented in [Burn et al. \(2021\)](#). Using 50% detection probability limits, 48 out of a total of 1000

systems would result in a single detection. Out of those, we show in Fig. 11 the three simulations that result in planets closest to Wolf 1069 b on the period-versus-mass plane. Simulations leading to a single planet detection went through a stage of giant impacts reducing the number of planets in the inner system and increasing the mass of the detectable planet with respect to the rest of the system. This is exemplified by the three best-fitting simulations which show three to four mergers with embryos more massive than the lunar mass.

While the scenario of the formation of a single planet cannot be ruled out, those simulations show that it is also possible in $\sim 5\%$ of the cases to form a seemingly lone planet if multiple embryos formed at the same time. However, if future observations extend the detection limits to larger orbits and lower planetary masses, this formation theory will be more severely challenged. While a single, late stage giant impact with a similarly massive body is currently in agreement with observations (e.g., Sim 650), this could be ruled out with better sensitivity. Then, a more dynamic history of the system is required (as in Sim 967 where the complete inner system was ejected or accreted by the detectable planet). A handicap of particular importance for thorough analyses of planet multiplicity is the omission of early core formation phases in current formation models (see e.g., [Ormel 2017](#); [Schlecker et al. 2021](#)). Future planet population synthesis studies have to take into account dust evolution, planetesimal formation, and planetary embryo formation in a self-consistent manner ([Voelkel et al. 2020, 2021](#)).

As for the observational prospects, dedicated measurements with a high-precision spectrograph focused on searching for sub-Earth-mass planets in the Wolf 1069 system could shed light on a potential inner planet candidate (as was the case with Proxima Centauri [d] first identified by [Suárez Mascareño et al. 2020](#) and later announced as a convincing planet candidate by [Faria et al. 2022](#), with a periodicity of ~ 5.12 d and $K \sim 40$ cm s $^{-1}$), or even further rule out this possibility.

5.3. Radio emission from star-planet interaction

Auroral radio emission from stars and planets is due to the electron cyclotron maser (ECM) instability ([Melrose & Dulk 1982](#)), whereby plasma processes within the star (or planet) magnetosphere generate a population of unstable electrons that amplifies the emission. The characteristic frequency of the ECM emission is given by the electron gyrofrequency, $\nu_G = 2.8 B$ MHz/G, where B is the local magnetic field in the source region in Gauss. ECM emission is a coherent mechanism that yields broadband ($\Delta\nu \sim \nu_G/2$), highly polarized (sometimes reaching 100%), amplified nonthermal radiation.

For Jupiter-like planets, which have magnetic fields of $B_{pl} \approx 10$ G, the direct detection of radio emission from them is plausible, as the associated gyrosynchrotron frequency falls above the ≈ 10 MHz ionosphere cutoff. However, the detection of radio emission from Earth-sized exoplanets, which are also the type of planets comprising a large majority of the CARMENES sample, is doomed to fail, as the associated frequency falls below the ionosphere cutoff.

Fortunately, if the velocity, v_{rel} , of the plasma relative to the planetary body is less than the Alfvén speed, v_A , in other words $M_A = v_{rel}/v_A < 1$, where M_A is the Alfvén Mach number, then energy and momentum can be transported upstream of the flow along Alfvén wings. Jupiter’s interaction with its Galilean satellites is a well-known example of sub-Alfvénic interaction, producing auroral radio emission ([Zarka 2007](#)). In the case of

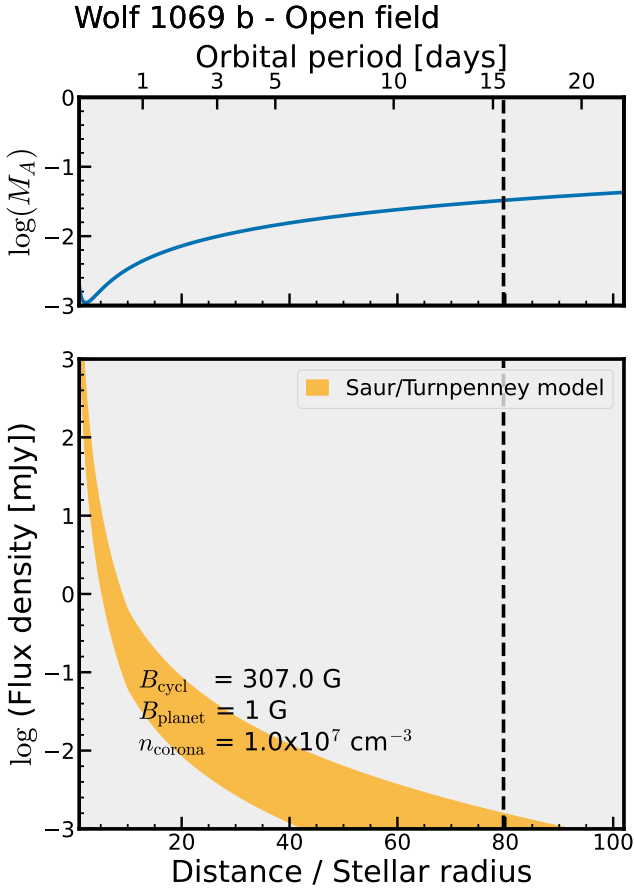


Fig. 12. Expected flux density for auroral radio emission arising from star-planet interaction in the system Wolf 1069, as a function of orbital distance. The interaction is expected to be in the sub-Alfvénic regime (i.e., $M_A = v_{\text{rel}}/v_{\text{Alfv}} \leq 1$; top panel) at the location of each planet (vertical dashed line).

star-planet interaction, the radio emission arises from the magnetosphere of the host star, induced by the exoplanet crossing the star magnetosphere, and the relevant magnetic field is that of the star, B_* , not the exoplanet magnetic field. Since M-dwarf stars have magnetic fields ranging from about 100 G and up to above 2–3 kG, their auroral emission falls in the range from a few hundred MHz up to a few GHz. This interaction is expected to yield detectable auroral radio emission via the cyclotron emission mechanism (e.g., Turnpenney et al. 2018; Pérez-Torres et al. 2021).

We followed the prescriptions in Appendix B of Pérez-Torres et al. (2021) to estimate the flux density expected to arise from the interaction between the planet Wolf 1069 b and its host star at a frequency of 860 MHz, which corresponds to the cyclotron frequency of the star magnetic field of 307 G, from Reiners et al. (2022). We computed the radio emission arising from star-planet interaction for two different magnetic field geometries: a closed dipolar geometry, and an open Parker spiral geometry. For the dipolar case, the motion of the plasma relative to Wolf 1069 b happens in the supra-Alfvénic regime. Therefore no energy or momentum can be transferred to the star through Alfvén waves. In the open Parker spiral case, however, the plasma motion proceeds in the sub-Alfvénic regime. We show in Fig. 12 the predicted flux density as a function of orbital distance arising from the interaction of a magnetized exoplanet (1 G) with its host star. The yellow shaded areas encompass the range of values from 0.01 to 0.1 for the efficiency factor, ϵ , in converting Poynting

flux into ECM radio emission. The expected flux density is less than $2 \mu\text{Jy}$. This is an extremely low value, which is not within the reach of even the most sensitive radio interferometers. The reasons behind this extremely faint signal are mainly two: First, the relatively large distance to the system (9.6 pc away); and second, the large separation of the planet from its host star (about 80 stellar radii). Therefore, the chances of detecting radio emission from star-planet interaction in Wolf 1069 are essentially null.

6. Conclusion

Using CARMENES spectroscopic measurements, we presented the discovery of a nontransiting exoplanet, Wolf 1069 b, with a period of $15.564 \pm 0.015 \text{ d}$, minimum mass of $1.26 \pm 0.21 M_{\oplus}$, and insolation of $0.652^{+0.029}_{-0.027} S_{\oplus}$, putting it safely in the conservative HZ around a low-mass M-dwarf star. This makes Wolf 1069 b the sixth closest ($d \sim 9.6 \text{ pc}$), Earth-mass planet in the conservative HZ from us, following Proxima Centauri b, GJ 1061 d, Teegarden’s Star c, and GJ 1002 b and c. Preliminary investigations of the potential habitability of the planet using GCM climate simulations suggest the planet to be a promising addition to the group of current targets to search for biosignature markers, such as Proxima Centauri b, TRAPPIST-1 e, and TOI-700 d. Wolf 1069 b unfortunately does not transit its stellar host, though future observations with thermal emission and reflected light phase curves could shed light on the properties of its atmosphere. We additionally investigated whether star-planet interactions in Wolf 1069 would be feasible to observe with radio emissions, but found these potential observations unfruitful.

The Wolf 1069 system becomes more intriguing as there is no significant evidence of closer-in planets ($P < 10 \text{ d}$) greater than one Earth mass, based on our detectability limits. This configuration is a plausible outcome based on a select few synthetic planetary population simulations, and even suggestive of a planet formation history including a late giant impact phase. The detection of potential inner sub-Earth-mass planets with further sub- m s^{-1} RV observations could then confirm or reject this formation theory.

The stellar host itself is a relatively inactive, low-mass M5.0 dwarf, though exhibits periods of higher activity levels, for which we determine its photometric rotation period to be 150–170 d. This rotation period was also present in the CARMENES RVs, and thus, modeled with a dSHO-GP in the final fit. The RVs showed one more additional significant periodicity at 90.3 d with a low amplitude (i.e., $< 1 \text{ m s}^{-1}$), however, we demonstrate that there is currently not enough supporting evidence in favor of a planetary origin and it appears to be an effect of telluric contamination. Further RV investigation could be beneficial. To conclude, Wolf 1069 b is a noteworthy discovery that will allow further exploration into the habitability of Earth-mass planets around M dwarfs, as well as case study in testing planetary formation theories.

Acknowledgements. Part of this work was supported by the German Deutsche Forschungsgemeinschaft, DFG project number Ts 17/2–1. CARMENES is an instrument at the Centro Astronómico Hispano-Alemán (CAHA) at Calar Alto (Almería, Spain), operated jointly by the Junta de Andalucía and the Instituto de Astrofísica de Andalucía (CSIC). CARMENES was funded by the Max-Planck-Gesellschaft (MPG), the Consejo Superior de Investigaciones Científicas (CSIC), the Ministerio de Economía y Competitividad (MINECO) and the European Regional Development Fund (ERDF) through projects FICTS-2011-02, ICTS-2017-07-CAHA-4, and CAHA16-CE-3978, and the members of the CARMENES Consortium (Max-Planck-Institut für Astronomie, Instituto de Astrofísica de Andalucía, Landessternwarte Königstuhl, Institut de Ciències de l’Espai, Institut für Astrophysik Göttingen, Universidad Complutense de Madrid, Thüringer Landessternwarte Tautenburg, Instituto de Astrofísica de Canarias,

Hamburger Sternwarte, Centro de Astrobiología and Centro Astronómico Hispano-Alemán), with additional contributions by the MINECO, the Deutsche Forschungsgemeinschaft through the Major Research Instrumentation Programme and Research Unit FOR2544 “Blue Planets around Red Stars”, the Klaus Tschira Stiftung, the states of Baden-Württemberg and Niedersachsen, and by the Junta de Andalucía. This work was based on data from the CARMENES data archive at CAB (CSIC-INTA). Data were partly collected with the 90 cm and 150 cm telescopes at Observatorio de Sierra Nevada (OSN), operated by the Instituto de Astrofísica de Andalucía (IAA, CSIC); we deeply acknowledge the OSN telescope operators for their very appreciable support. The Telescopi Joan Oró (TJO) of the Observatori Astronòmic del Montsec is owned by the Generalitat de Catalunya and operated by the Institut d’Estudis Espacials de Catalunya (IEEC). We acknowledge financial support from the Agencia Estatal de Investigación of the Ministerio de Ciencia e Innovación (AEI/10.13039/501100011033) and the ERDF “A way of making Europe” through projects PID2019-109522GB-C5[1:4], PID2019-107061GB-C64, and PID2019-110689RB-100, and the Centre of Excellence “Severo Ochoa” and “María de Maeztu” awards to the Instituto de Astrofísica de Canarias (SEV-2015-0548), Instituto de Astrofísica de Andalucía (SEV-2017-0709), and Centro de Astrobiología (MDM-2017-0737); the European Research Council under the Horizon 2020 Framework Program (ERC Advanced Grant Origins 832428 and under Marie Skłodowska-Curie grant 895525); the Generalitat de Catalunya/CERCA programme; the DFG through the priority program SPP 1992 “Exploring the Diversity of Extrasolar Planets (JE 701/5-1)” and the Research Unit FOR 2544 “Blue Planets around Red Stars” (KU 3625/2-1); the Bulgarian National Science Fund through program “VIHREN-2021” (KP-06-DV/5); the SNSF under grant P2BEP2_195285; the National Science Foundation under award No. 1753373, and by a Clare Boothe Luce Professorship. We thank the anonymous referee for the insightful comments that helped improve the quality of this paper. Software: *astropy* (Astropy Collaboration 2018), *celerite* (Foreman-Mackey et al. 2017), *Exo-Striker* (Trifonov 2019), *dynesty* (Speagle & Barbary 2018; Speagle 2020), *george* (Ambikasaran et al. 2015), *juliet* (Espinoza et al. 2019), *matplotlib* (Hunter 2007), *numpy* (Oliphant 2006), *pandas* (The pandas development team 2020), *PyFITS* (Barrett et al. 2012), *raccoon* (Lafarga et al. 2020), *radvel* (Fulton et al. 2018), *serval* (Zechmeister et al. 2018) *scipy* (Virtanen et al. 2020).

References

- Amado, P. J., Bauer, F. F., Rodríguez López, C., et al. 2021, *A&A*, **650**, A188
- Ambikasaran, S., Foreman-Mackey, D., Greengard, L., Hogg, D. W., & O’Neil, M. 2015, *IEEE Trans. Pattern Anal. Mach. Intell.*, **38**, 252
- Anglada-Escudé, G., Tuomi, M., Gerlach, E., et al. 2013, *A&A*, **556**, A126
- Anglada-Escudé, G., Amado, P. J., Barnes, J., et al. 2016, *Nature*, **536**, 437
- Astropy Collaboration (Price-Whelan, A. M., et al.) 2018, *AJ*, **156**, 123
- Baluev, R. V. 2009, *MNRAS*, **393**, 969
- Barrett, P., Hsu, J. C., Hanley, C., et al. 2012, *PyFITS: Python FITS Module*
- Bidelman, W. P. 1985, *ApJS*, **59**, 197
- Bluhm, P., Luque, R., Espinoza, N., et al. 2020, *A&A*, **639**, A132
- Bonfils, X., Delfosse, X., Udry, S., et al. 2013, *A&A*, **549**, A109
- Bonfils, X., Astudillo-Defru, N., Díaz, R., et al. 2018, *A&A*, **613**, A25
- Brady, M., & Bean, J. 2022, *AJ*, **163**, 255
- Burn, R., Schlecker, M., Mordasini, C., et al. 2021, *A&A*, **656**, A72
- Butters, O. W., West, R. G., Anderson, D. R., et al. 2010, *A&A*, **520**, L10
- Caballero, J. A., Cortés-Contreras, M., Alonso-Floriano, F. J., et al. 2016a, in 19th Cambridge Workshop on Cool Stars, Stellar Systems, and the Sun (CS19), 148
- Caballero, J. A., Guàrdia, J., López del Fresno, M., et al. 2016b, *SPIE Conf. Ser.*, **9910**, 99100E
- Chadney, J. M., Galand, M., Koskinen, T. T., et al. 2016, *A&A*, **587**, A87
- Cifuentes, C., Caballero, J. A., Cortés-Contreras, M., et al. 2020, *A&A*, **642**, A115
- Cohen, O., Drake, J. J., Glocer, A., et al. 2014, *ApJ*, **790**, 57
- Collins, K. A., Kielkopf, J. F., Stassun, K. G., & Hessman, F. V. 2017, *AJ*, **153**, 77
- Colome, J., & Ribas, I. 2006, *IAU Special Session*, **6**, 11
- Cutri, R. M., et al. 2012, *VizieR Online Data Catalog: II/311*
- Cutri, R. M., et al. 2014, *VizieR Online Data Catalog: II/328*
- David, T. J., Petigura, E. A., Luger, R., et al. 2019, *ApJ*, **885**, L12
- Dawson, R. I., & Fabrycky, D. C. 2010, *ApJ*, **722**, 937
- Del Genio, A. D., Way, M. J., Amundsen, D. S., et al. 2019a, *Astrobiology*, **19**, 99
- Del Genio, A. D., Way, M. J., Kiang, N. Y., et al. 2019b, *ApJ*, **887**, 197
- Delrez, L., Murray, C. A., Pozuelos, F. J., et al. 2022, *A&A*, **667**, A59
- Dieterich, S. B., Henry, T. J., Golimowski, D. A., Krist, J. E., & Tanner, A. M. 2012, *AJ*, **144**, 64
- Díez Alonso, E., Caballero, J. A., Montes, D., et al. 2019, *A&A*, **621**, A126
- Dobos, V., Haris, A., Kamp, I. E. E., & van der Tak, F. F. S. 2022, *MNRAS*, **513**, 5290
- Dole, S. H. 1964, *Habitable Planets for Man* (USA: RAND Corporation)
- Dong, C., Jin, M., Lingam, M., et al. 2018, *Proc. Natl. Acad. Sci.*, **115**, 260
- Dreizler, S., Jeffers, S. V., Rodríguez, E., et al. 2020, *MNRAS*, **493**, 536
- Dressing, C. D., & Charbonneau, D. 2015, *ApJ*, **807**, 45
- Eastman, J., Gaudi, B. S., & Agol, E. 2013, *PASP*, **125**, 83
- Edson, A. R., Kasting, J. F., Pollard, D., Lee, S., & Bannon, P. R. 2012, *Astrobiology*, **12**, 562
- Espinoza, N., Kossakowski, D., & Brahm, R. 2019, *MNRAS*, **490**, 2262
- Faria, J. P., Suárez Mascareño, A., Figueira, P., et al. 2022, *A&A*, **658**, A115
- Faucher, T. J., Turbet, M., Villanueva, G. L., et al. 2019, *ApJ*, **887**, 194
- Feroz, F., & Hobson, M. P. 2014, *MNRAS*, **437**, 3540
- Feroz, F., Balan, S. T., & Hobson, M. P. 2011, *MNRAS*, **415**, 3462
- Foreman-Mackey, D., Agol, E., Ambikasaran, S., & Angus, R. 2017, *AJ*, **154**, 220
- Fuhrmeister, B., Czesla, S., Hildebrandt, L., et al. 2020, *A&A*, **640**, A52
- Fuhrmeister, B., Czesla, S., Nagel, E., et al. 2022, *A&A*, **657**, A125
- Fulton, B. J., Petigura, E. A., Blunt, S., & Sinukoff, E. 2018, *PASP*, **130**, 044504
- Gaia Collaboration (Vallenari, A., et al.) 2023, *A&A*, in press, <https://doi.org/10.1051/0004-6361/202243940>
- Gardner, J. P., Mather, J. C., Clampin, M., et al. 2009, *Astrophys. Space Sci. Proc.*, **10**, 1
- Gibbs, A., Bixel, A., Rackham, B. V., et al. 2020, *AJ*, **159**, 169
- Gillen, E., Briegal, J. T., Hodgkin, S. T., et al. 2020, *MNRAS*, **492**, 1008
- Gliese, W. 1957, *Astron. Rechen-Institut, Heidelberg*, **89**, 8
- Gliese, W., & Jahreiß, H. 1979, *A&AS*, **38**, 423
- Hardegree-Ullman, K. K., Cushing, M. C., Muirhead, P. S., & Christiansen, J. L. 2019, *VizieR Online Data Catalog: J/AJ/158/75*
- Heller, R., Leconte, J., & Barnes, R. 2011, *A&A*, **528**, A27
- Hilton, E. J. 2011, PhD thesis, University of Washington, Seattle, USA
- Hipke, M., & Heller, R. 2019, *A&A*, **623**, A39
- Hsu, D. C., Ford, E. B., & Terrien, R. 2020, *MNRAS*, **498**, 2249
- Hunter, J. D. 2007, *Comput. Sci. Eng.*, **9**, 90
- Irwin, J. M., Berta-Thompson, Z. K., Charbonneau, D., et al. 2015, in Cambridge Workshop on Cool Stars, Stellar Systems, and the Sun, **18**, 767
- Jacobson, S. A., Rubie, D. C., Hernlund, J., Morbidelli, A., & Nakajima, M. 2017, *Earth Planet. Sci. Lett.*, **474**, 375
- Janson, M., Bergfors, C., Brandner, W., et al. 2014, *ApJ*, **789**, 102
- Jeffers, S. V., Barnes, J. R., Schöfer, P., et al. 2022, *A&A*, **663**, A27
- Jenkins, J. S., Ramsey, L. W., Jones, H. R. A., et al. 2009, *ApJ*, **704**, 975
- Jenkins, J. M., Twicken, J. D., McCauliff, S., et al. 2016, *SPIE Conf. Ser.*, **9913**, 99133E
- Jódar, E., Pérez-Garrido, A., Díaz-Sánchez, A., et al. 2013, *MNRAS*, **429**, 859
- Kasper, M., Cerpa Urra, N., Pathak, P., et al. 2021, *The Messenger*, **182**, 38
- Kasting, J. F., Whitmire, D. P., & Reynolds, R. T. 1993, *Icarus*, **101**, 108
- Kemmer, J., Stock, S., Kossakowski, D., et al. 2020, *A&A*, **642**, A236
- Kopparapu, R. K., Ramirez, R., Kasting, J. F., et al. 2013, *ApJ*, **765**, 131
- Kopparapu, R. K., Ramirez, R. M., Schottelkotte, J., et al. 2014, *ApJ*, **787**, L29
- Kopparapu, R. K., Wolf, E. T., & Meadows, V. S. 2020, in *Planetary Astrobiology*, eds. V. S. Meadows, G. N. Arney, B. E. Schmidt, & D. J. Des Marais (Tucson: University of Arizona Press), 449
- Kossakowski, D., Kemmer, J., Bluhm, P., et al. 2021, *A&A*, **656**, A124
- Lafarga, M., Ribas, I., Lovis, C., et al. 2020, *A&A*, **636**, A36
- Lafarga, M., Ribas, I., Reiners, A., et al. 2021, *A&A*, **652**, A28
- Lam, K. W. F., Csizmadia, S., Astudillo-Defru, N., et al. 2021, *Science*, **374**, 1271
- Lamman, C., Baranec, C., Berta-Thompson, Z. K., et al. 2020, *AJ*, **159**, 139
- Leconte, J., Forget, F., Charnay, B., et al. 2013, *A&A*, **554**, A69
- Luque, R., & Pallé, E. 2022, *Science*, **377**, 1211
- Luyten, W. J. 1955, *Luyten’s Five Tenth*
- Maiolino, R., Haehnelt, M., Murphy, M. T., et al. 2013, *ArXiv e-prints* [arXiv:1310.3163]
- Mann, A. W., Feiden, G. A., Gaidos, E., Boyajian, T., & von Braun, K. 2015, *ApJ*, **804**, 64
- Marfil, E., Tabernero, H. M., Montes, D., et al. 2021, *A&A*, **656**, A162
- Martínez-Rodríguez, H., Caballero, J. A., Cifuentes, C., Piro, A. L., & Barnes, R. 2019, *ApJ*, **887**, 261
- Melrose, D. B., & Dulk, G. A. 1982, *ApJ*, **259**, 844
- Montes, D., López-Santiago, J., Gálvez, M. C., et al. 2001, *MNRAS*, **328**, 45
- Mulders, G. D., Pascucci, I., & Apai, D. 2015, *ApJ*, **814**, 130
- Mulders, G. D., Drażkowska, J., van der Marel, N., Ciesla, F. J., & Pascucci, I. 2021, *ApJ*, **920**, L1
- Nagel, E., Czesla, S., Kaminski, A., et al. 2022, *A&A*, submitted
- Newton, E. R., Irwin, J., Charbonneau, D., et al. 2016, *ApJ*, **821**, 93
- Newton, E. R., Irwin, J., Charbonneau, D., et al. 2017, *ApJ*, **834**, 85
- Oliphant, T. E. 2006, *A Guide to NumPy* (USA: Trelgol Publishing),
- Ormel, C. W. 2017, *Astrophys. Space Sci. Lib.*, **445**, 197

- Pasegger, V. M., Schweitzer, A., Shulyak, D., et al. 2019, *A&A*, **627**, A161
- Pérez-Torres, M., Gómez, J. F., Ortiz, J. L., et al. 2021, *A&A*, **645**, A77
- Perryman, M. 2018, *The Exoplanet Handbook* (Cambridge: Cambridge University Press)
- Pollacco, D. L., Skillen, I., Collier Cameron, A., et al. 2006, *PASP*, **118**, 1407
- Pollack, J. B., Hubickij, O., Bodenheimer, P., et al. 1996, *Icarus*, **124**, 62
- Probst, R. G. 1983, *ApJS*, **53**, 335
- Quirrenbach, A., Amado, P. J., Caballero, J. A., et al. 2014, *Proc. SPIE*, **9147**, 91471F
- Quirrenbach, A., Amado, P. J., Ribas, I., et al. 2018, *SPIE Conf. Ser.*, **10702**, 107020W
- Rajpurohit, A. S., Allard, F., Rajpurohit, S., et al. 2018, *A&A*, **620**, A180
- Reid, I. N., Hawley, S. L., & Gizis, J. E. 1995, *AJ*, **110**, 1838
- Reiners, A., Zechmeister, M., Caballero, J. A., et al. 2018, *A&A*, **612**, A49
- Reiners, A., Shulyak, D., Käpylä, P. J., et al. 2022, *A&A*, **662**, A41
- Ribas, I., Reiners, A., Zechmeister, M., et al. 2023, *A&A*, in press, <https://doi.org/10.1051/0004-6361/202244879>
- Ricker, G. R., Winn, J. N., Vanderspek, R., et al. 2015, *J. Astron. Teles. Instrum. Syst.*, **1**, 014003
- Robertson, P., & Mahadevan, S. 2014, *ApJ*, **793**, L24
- Rodríguez, E., García, J. M., Costa, V., et al. 2010, *MNRAS*, **408**, 2149
- Rojas-Ayala, B., Covey, K. R., Muirhead, P. S., & Lloyd, J. P. 2012, *ApJ*, **748**, 93
- Sabotta, S., Schlecker, M., Chaturvedi, P., et al. 2021, *A&A*, **653**, A114
- Schlecker, M., Pham, D., Burn, R., et al. 2021, *A&A*, **656**, A73
- Schlecker, M., Burn, R., Sabotta, S., et al. 2022, *A&A*, **664**, A180
- Schöfer, P., Jeffers, S. V., Reiners, A., et al. 2019, *A&A*, **623**, A44
- Schweitzer, A., Pasegger, V. M., Cifuentes, C., et al. 2019, *A&A*, **625**, A68
- Seager, S. 2010, *Exoplanets* (Tucson, AZ: University of Arizona Press)
- Sebastian, D., Gillon, M., Ducrot, E., et al. 2021, *A&A*, **645**, A100
- Segura, A., Krellove, K., Kasting, J. F., et al. 2003, *Astrobiology*, **3**, 689
- Segura, A., Walkowicz, L. M., Meadows, V., Kasting, J., & Hawley, S. 2010, *Astrobiology*, **10**, 751
- Sestovic, M., & Demory, B.-O. 2020, *A&A*, **641**, A170
- Shields, A. L., Ballard, S., & Johnson, J. A. 2016, *Phys. Rep.*, **663**, 1
- Shporer, A., Collins, K. A., Astudillo-Defru, N., et al. 2020, *ApJ*, **890**, L7
- Skrutskie, M. F., Cutri, R. M., Stiening, R., et al. 2006, *AJ*, **131**, 1163
- Smette, A., Sana, H., Noll, S., et al. 2015, *A&A*, **576**, A77
- Smith, J. C., Stumpe, M. C., Van Cleve, J. E., et al. 2012, *PASP*, **124**, 1000
- Speagle, J., & Barbary, K. 2018, *Astrophysics Source Code Library* [[record ascl:1809.013](https://doi.org/10.26434/chemrxiv-2018-0131)]
- Speagle, J. S. 2020, *MNRAS*, **493**, 3132
- Stelzer, B., Marino, A., Micela, G., López-Santiago, J., & Liefke, C. 2013, *MNRAS*, **431**, 2063
- Stock, S., & Kemmer, J. 2020, *J. Open Source Softw.*, **5**, 1771
- Stock, S., Nagel, E., Kemmer, J., et al. 2020, *A&A*, **643**, A112
- Stumpe, M. C., Smith, J. C., Van Cleve, J. E., et al. 2012, *PASP*, **124**, 985
- Stumpe, M. C., Smith, J. C., Catanzarite, J. H., et al. 2014, *PASP*, **126**, 100
- Suárez Mascareño, A., Faria, J. P., Figueira, P., et al. 2020, *A&A*, **639**, A77
- Suárez Mascareño, A., González-Álvarez, E., Zapatero Osorio, M. R., et al. 2023, *A&A*, **670**, A5
- Suissa, G., Wolf, E. T., Kopparapu, R. k., et al. 2020, *AJ*, **160**, 118
- Tamuz, O., Mazeh, T., & Zucker, S. 2005, *MNRAS*, **356**, 1466
- Terrier, R. C., Mahadevan, S., Deshpande, R., & Bender, C. F. 2015, *ApJS*, **220**, 16
- The pandas development team 2020, <https://github.com/pandas-dev/pandas>
- Trifonov, T. 2019, *Astrophysics Source Code Library* [[record ascl:1906.004](https://doi.org/10.26434/chemrxiv-2019-004)]
- Trifonov, T., Tal-Or, L., Zechmeister, M., et al. 2020, *A&A*, **636**, A74
- Trotta, R. 2008, *Contemp. Phys.*, **49**, 71
- Turbet, M., Leconte, J., Selsis, F., et al. 2016, *A&A*, **596**, A112
- Turbet, M., Bolmont, E., Leconte, J., et al. 2018, *A&A*, **612**, A86
- Turbet, M., Fauchez, T. J., Sergeev, D. E., et al. 2022, *Planet. Sci. J.*, **3**, 211
- Turnpenney, S., Nichols, J. D., Wynn, G. A., & Burleigh, M. R. 2018, *ApJ*, **854**, 72
- Virtanen, P., Gommers, R., Oliphant Travis E., et al. 2020, *Nat. Methods*, **17**, 261
- Voelkel, O., Klahr, H., Mordasini, C., Emsenhuber, A., & Lenz, C. 2020, *A&A*, **642**, A75
- Voelkel, O., Deienno, R., Kretke, K., & Klahr, H. 2021, *A&A*, **645**, A131
- Way, M. J., Aleinov, I., Amundsen, D. S., et al. 2017, *ApJS*, **231**, 12
- Weis, E. W. 1984, *ApJS*, **55**, 289
- Wolf, E. T. 2017, *ApJ*, **839**, L1
- Wolf, E. T., Kopparapu, R., Haqq-Misra, J., & Fauchez, T. J. 2022, *Planet. Sci. J.*, **3**, 7
- Wolf, M. 1920, *Astron. Nachr.*, **212**, 303
- Wood, B. E., Brown, A., Linsky, J. L., et al. 1994, *ApJS*, **93**, 287
- Yang, J., Abbot, D. S., Koll, D. D. B., Hu, Y., & Showman, A. P. 2019, *ApJ*, **871**, 29
- Zacharias, N., Finch, C. T., Girard, T. M., et al. 2012, *VizieR Online Data Catalog: I/322A*
- Zarka, P. 2007, *Planet. Space Sci.*, **55**, 598
- Zechmeister, M., & Kürster, M. 2009, *A&A*, **496**, 577
- Zechmeister, M., Kürster, M., & Endl, M. 2009, *A&A*, **505**, 859
- Zechmeister, M., Reiners, A., Amado, P. J., et al. 2018, *A&A*, **609**, A12
- Zechmeister, M., Dreizler, S., Ribas, I., et al. 2019, *A&A*, **627**, A49
- Zeng, L., Sasselov, D. D., & Jacobsen, S. B. 2016, *ApJ*, **819**, 127

- ¹ Max-Planck-Institut für Astronomie, Königstuhl 17, 69117 Heidelberg, Germany
e-mail: astrodianakossakowski@gmail.com
- ² Department of Astronomy, Sofia University “St Kliment Ohridski”, 5 James Bourchier Blvd, 1164 Sofia, Bulgaria
- ³ Landessternwarte, Zentrum für Astronomie der Universität Heidelberg, Königstuhl 12, 69117 Heidelberg, Germany
- ⁴ Centro de Astrobiología (CSIC-INTA), ESAC, Camino bajo del castillo s/n, 28692 Villanueva de la Cañada, Madrid, Spain
- ⁵ NASA Goddard Space Flight Center, 8800 Greenbelt Road, Greenbelt, MD 20771, USA
- ⁶ Department of Astronomy, University of Maryland, College Park, MD 20742, USA
- ⁷ Center for Research and Exploration in Space Science and Technology, NASA/GSFC, Greenbelt, MD 20771, USA
- ⁸ American University, College of Arts and Sciences, Washington DC, USA
- ⁹ Hamburger Sternwarte, Gojenbergsweg 112, 21029 Hamburg, Germany
- ¹⁰ Thüringer Landessternwarte Tautenburg, Sternwarte 5, 07778 Tautenburg, Germany
- ¹¹ Institut de Ciències de l’Espai (ICE, CSIC), Campus UAB, C/ de Can Magrans s/n, 08193 Cerdanyola del Vallès, Spain
- ¹² Institut d’Estudis Espacials de Catalunya (IEEC), C/ Gran Capità 2-4, 08034 Barcelona, Spain
- ¹³ Instituto de Astrofísica de Andalucía (CSIC), Glorieta de la Astronomía s/n, 18008 Granada, Spain
- ¹⁴ Centro de Astrobiología (CSIC-INTA), Carretera de Ajalvir km 4, 28850 Torrejón de Ardoz, Madrid, Spain
- ¹⁵ Institut für Astrophysik und Geophysik, Georg-August-Universität, Friedrich-Hund-Platz 1, 37077 Göttingen, Germany
- ¹⁶ Centro Astronómico Hispano en Andalucía, Observatorio de Calar Alto, Sierra de los Filabres, 04550 Gérgal, Spain
- ¹⁷ Instituto de Astrofísica de Canarias (IAC), 38200 La Laguna, Tenerife, Spain
- ¹⁸ Departamento de Astrofísica, Universidad de La Laguna, 38206 La Laguna, Tenerife, Spain
- ¹⁹ Max-Planck-Institut für Sonnensystemforschung, Justus-von-Liebig Weg 3, 37077 Göttingen, Germany
- ²⁰ Department of Physics, University of Warwick, Gibbet Hill Road, Coventry CV4 7AL, UK
- ²¹ Departamento de Física de la Tierra y Astrofísica & IPARCOS-UCM (Instituto de Física de Partículas y del Cosmos de la UCM), Facultad de Ciencias Físicas, Universidad Complutense de Madrid, 28040 Madrid, Spain
- ²² Department of Physics, Ariel University, Ariel 40700, Israel
- ²³ School of Sciences, European University Cyprus, Diogenes street, Engomi, 1516 Nicosia, Cyprus
- ²⁴ Department of Astronomy/Steward Observatory, The University of Arizona, 933 North Cherry Avenue, Tucson, AZ 85721, USA
- ²⁵ Centre for Earth Evolution and Dynamics, Department of Geosciences, Universitetet i Oslo, Sem Sælands vei 2b, 0315 Oslo, Norway
- ²⁶ Department of Physics & Astronomy, University of California, Irvine, CA 92697, USA
- ²⁷ University of Colorado, Boulder Laboratory for Atmospheric and Space Physics, Department of Atmospheric and Oceanic Sciences, Boulder, CO 80303, USA
- ²⁸ NASA NExSS Virtual Planetary Laboratory, Seattle, WA, USA

Appendix A: AliasFinder figures

The RV data show a variety of aliases related to the 15.6 d signal. In order to establish that 15.6 d is indeed the true periodicity, we tested the aliasing using AliasFinder (Stock & Kemmer 2020), which follows the methodology from Dawson & Fabrycky (2010). The essence behind the algorithm is to examine the GLS periodograms of simulated data sets, in which either of the two

aliasing signals are injected, to the GLS periodogram provided by the original data. The injected signal of whichever periodogram matches best to the original one is defined to be the true periodicity apparent in the data. The results of this method by simulating 1000 time series for both the daily and yearly sampling frequencies is shown in Fig. A.1, confirming the true signal to be 15.6 d.

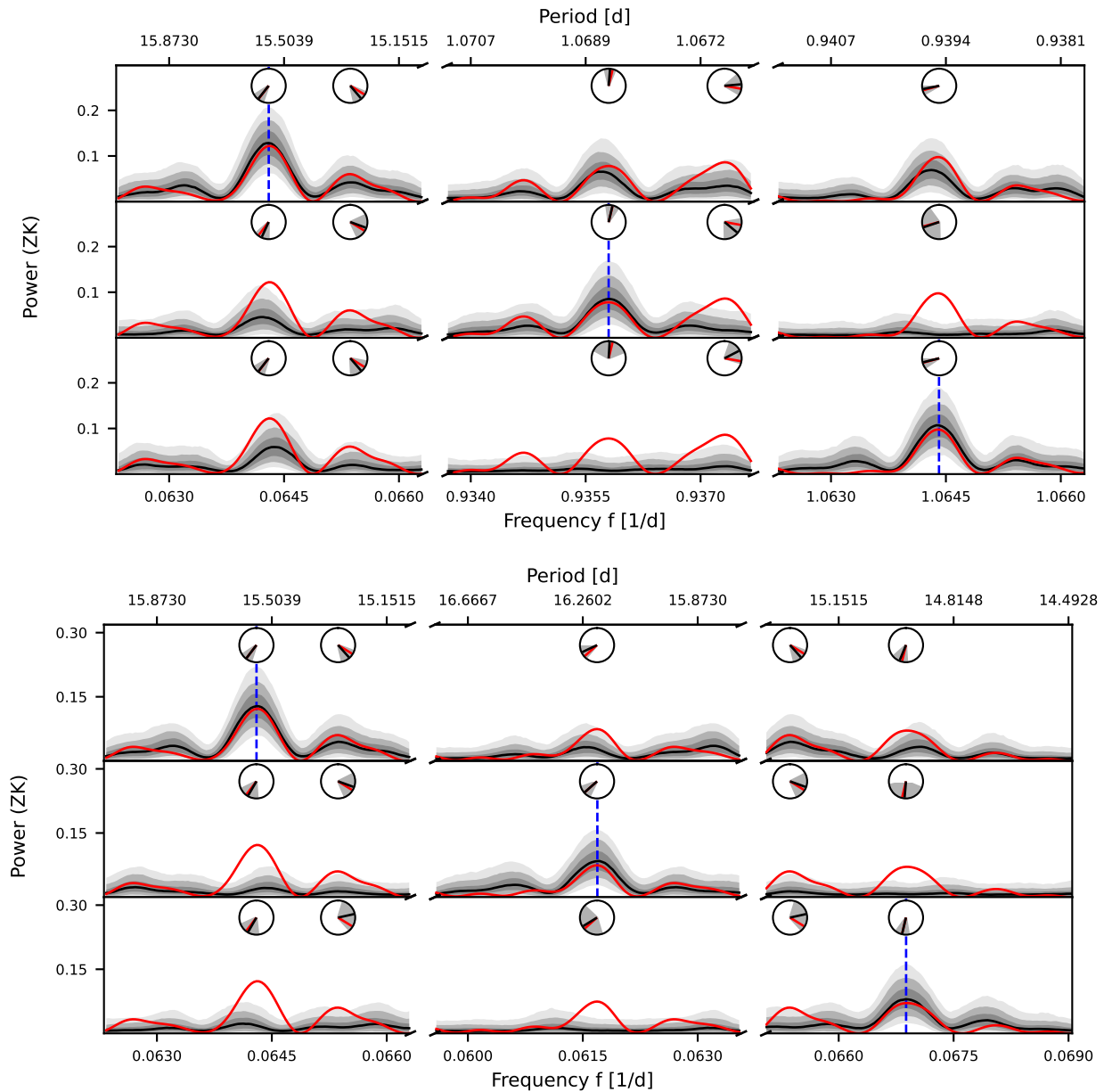


Fig. A.1. Plots generated by AliasFinder for the daily (*top*) and yearly (*bottom*) aliases for the 15.6 d signal. Each row illustrates the results for one simulated frequency, as indicated by the dashed blue vertical line. Each column is centered on a frequency window corresponding to the simulated frequencies. The red line represents the periodogram of the original data set, whereas the black line is the median of the simulations, and the gray shaded regions depict the interquartile range and the confidence range of 90% and 99% of the simulations. The clock diagrams indicate the phase.

Appendix B: Known planets in the habitable zone around M dwarfs

We started from the list collected by PHL at UPR, which obtains its parameters from the NASA exoplanet archive. The list, as last updated on 06 December 2021, comprises 21 planets that are most probable to have a rocky composition and maintain surface liquid water. We individually vetted each system using the most up-to-date literature and updated the planetary and stellar parameters. Most of the planets stayed consistent since the update, though there are some modifications:

- **GJ 667 C**: We omit the planets d, e, f, and g proposed by [Anglada-Escudé et al. \(2013\)](#) in which the second two would reside in the HZ. They emerged as controversial when stellar activity was also modeled within the RVs as a red-noise component ([Robertson & Mahadevan 2014](#); [Feroz & Hobson 2014](#)). Unfortunately, that leaves only planet c in the optimistic HZ in this planetary system. Nonetheless, there is still an inner planet to that of the HZ one, planet b, with a minimum mass of $5.6 M_{\oplus}$.
- **LP 890-9**: We add the planet b recently unveiled by [Delrez et al. \(2022\)](#) around LP 890-9, which is next coolest star found to host a HZ planet, after TRAPPIST-1.
- **GJ 1002**: We add planets b and c recently discovered around the M5.5 V star, both of which reside in the conservative HZ ([Suárez Mascareño et al. 2023](#)).

Appendix C: Priors and posteriors

Table C.1. Prior parameters for the photometric rotation period determination in Sect. 3.2.

Parameter name	Prior	Unit	Description
<i>Photometric instrumental parameters</i>			
$\mu_{\text{OSN-V-T150}}$	$\mathcal{U}(0.9, 1.1)$	ppm	Photometric normalization for OSN-V-T150
$\sigma_{\text{OSN-V-T150}}$	$\mathcal{J}(10^{-8}, 10^{-1})$	ppm	Extra jitter term for OSN-V-T150
$\mu_{\text{OSN-R-T150}}$	$\mathcal{U}(0.9, 1.1)$	ppm	Photometric normalization for OSN-R-T150
$\sigma_{\text{OSN-R-T150}}$	$\mathcal{J}(10^{-8}, 10^{-1})$	ppm	Extra jitter term for OSN-R-T150
$\mu_{\text{OSN-I-T150}}$	$\mathcal{U}(0.9, 1.1)$	ppm	Photometric normalization for OSN-I-T150
$\sigma_{\text{OSN-I-T150}}$	$\mathcal{J}(10^{-8}, 10^{-1})$	ppm	Extra jitter term for OSN-I-T150
$\mu_{\text{OSN-V-T90}}$	$\mathcal{U}(0.9, 1.1)$	ppm	Photometric normalization for OSN-V-T90
$\sigma_{\text{OSN-V-T90}}$	$\mathcal{J}(10^{-8}, 10^{-1})$	ppm	Extra jitter term for OSN-V-T90
$\mu_{\text{OSN-R-T90}}$	$\mathcal{U}(0.9, 1.1)$	ppm	Photometric normalization for OSN-R-T90
$\sigma_{\text{OSN-R-T90}}$	$\mathcal{J}(10^{-8}, 10^{-1})$	ppm	Extra jitter term for OSN-R-T90
$\mu_{\text{TJO-R}}$	$\mathcal{U}(0.9, 1.1)$	ppm	Photometric normalization for TJO-R
$\sigma_{\text{TJO-R}}$	$\mathcal{J}(10^{-8}, 10^{-1})$	ppm	Extra jitter term for TJO-R
$\mu_{\text{SuperWASP}}$	$\mathcal{U}(0.9, 1.1)$	ppm	Photometric normalization for SuperWASP
$\sigma_{\text{SuperWASP}}$	$\mathcal{J}(10^{-8}, 10^{-1})$	ppm	Extra jitter term for SuperWASP
$\mu_{\text{MEarth-tel01-s1}}$	$\mathcal{U}(0.9, 1.1)$	ppm	Photometric normalization for MEarth-tel01-s1
$\sigma_{\text{MEarth-tel01-s1}}$	$\mathcal{J}(10^{-8}, 10^{-1})$	ppm	Extra jitter term for MEarth-tel01-s1
$\mu_{\text{MEarth-tel01-s2}}$	$\mathcal{U}(0.9, 1.1)$	ppm	Photometric normalization for MEarth-tel01-s2
$\sigma_{\text{MEarth-tel01-s2}}$	$\mathcal{J}(10^{-8}, 10^{-1})$	ppm	Extra jitter term for MEarth-tel01-s2
$\mu_{\text{MEarth-tel05-s2}}$	$\mathcal{U}(0.9, 1.1)$	ppm	Photometric normalization for MEarth-tel05-s2
$\sigma_{\text{MEarth-tel05-s2}}$	$\mathcal{J}(10^{-8}, 10^{-1})$	ppm	Extra jitter term for MEarth-tel05-s2
<i>dSHO-GP parameters</i>			
$P_{\text{rot, GP, all}}^{(a)}$	$\mathcal{J}(10, 200)$	d	Primary period of the dSHO-GP
$\delta Q_{\text{GP, all}}^{(a)}$	$\mathcal{J}(10^2, 10^5)$...	Quality factor difference between the first and second oscillations of the dSHO-GP
$Q_{0 \text{ GP, all}}^{(a)}$	$\mathcal{J}(10^{-8}, 10^3)$...	Quality factor for the secondary oscillation of the dSHO-GP
$\sigma_{\text{GP, OSN-V-T150, OSN-V-T90}}$	$\mathcal{U}(0.0, 0.2)$...	Amplitude of the dSHO-GP
$\sigma_{\text{GP, OSN-R-T150, OSN-R-T90, TJO-R}}$	$\mathcal{U}(0.0, 0.2)$...	
$\sigma_{\text{GP, OSN-I-T150}}$	$\mathcal{U}(0.0, 0.2)$...	
$\sigma_{\text{GP, MEarth-tel01-s1}}$	$\mathcal{U}(0.0, 0.2)$...	
$\sigma_{\text{GP, MEarth-tel01-s2, MEarth-tel05-s2}}$	$\mathcal{U}(0.0, 0.2)$...	
$\sigma_{\text{GP, SuperWASP}}$	$\mathcal{U}(0.0, 0.2)$...	
$f_{\text{GP, OSN-V-T150, OSN-V-T90}}$	$\mathcal{U}(0.1, 1.0)$...	Fractional amplitude of the secondary oscillation of the dSHO-GP
$f_{\text{GP, OSN-R-T150, OSN-R-T90, TJO-R}}$	$\mathcal{U}(0.1, 1.0)$...	
$f_{\text{GP, OSN-I-T150}}$	$\mathcal{U}(0.1, 1.0)$...	
$f_{\text{GP, MEarth-tel01-s1, MEarth-tel01-s2, MEarth-tel05-s2}}$	$\mathcal{U}(0.1, 1.0)$...	
$f_{\text{GP, SuperWASP}}$	$\mathcal{U}(0.1, 1.0)$...	

Notes. ^(a)“all” comprises the following instruments: OSN-V-T150, OSN-R-T150, OSN-I-T150, OSN-V-T90, OSN-R-T90, TJO-R, SuperWASP, MEarth-tel01-s1, MEarth-tel01-s2, MEarth-tel05-s2

Table C.2. Priors for the RV fits for Wolf 1069 with *juliet* in Sect. 4.2.

Parameter name	Prior	Units	Description
<i>Parameters for planet b</i>			
P_b	$\mathcal{U}(15.4, 15.7)$	d	Period.
$t_{0,b}$	$\mathcal{U}(2458502.0, 2458515.0)$	d	Time-of-transit center.
K_b	$\mathcal{U}(0.0, 5.0)$	m s^{-1}	Radial velocity semi-amplitude.
$S_{1,b} = \sqrt{e_b} \sin \omega_b$	$\mathcal{F}(0.0)$ (circular)	...	Parametrization for e and ω
	$\mathcal{U}(-1, 1)$ (eccentric)	...	Parametrization for e and ω
$S_{2,b} = \sqrt{e_b} \cos \omega_b$	$\mathcal{F}(0.0)$ (circular)	...	Parametrization for e and ω
	$\mathcal{U}(-1, 1)$ (eccentric)	...	Parametrization for e and ω
<i>Parameters for the 90.3 d signal</i>			
P_2	$\mathcal{U}(85.0, 95.0)$	d	Period.
$t_{0,2}$	$\mathcal{U}(2458500.0, 2458590.0)$	d	Time-of-transit center.
K_2	$\mathcal{U}(0.0, 5.0)$	m s^{-1}	Radial velocity semi-amplitude.
$S_{1,2} = \sqrt{e_b} \sin \omega_b$	$\mathcal{F}(0.0)$ (circular)	...	Parametrization for e and ω
$S_{2,2} = \sqrt{e_b} \cos \omega_b$	$\mathcal{F}(0.0)$ (circular)	...	Parametrization for e and ω
<i>RV instrumental parameters</i>			
$\gamma_{\text{CARMENES-VIS}}$	$\mathcal{U}(-20.0, 20.0)$	m s^{-1}	Systemic velocity for CARMENES
$\sigma_{\text{CARMENES-VIS}}$	$\mathcal{J}(0.01, 50.0)$	m s^{-1}	Extra jitter term for CARMENES
<i>dSHO-GP parameters</i>			
$\sigma_{\text{GP, CARMENES-VIS}}$	$\mathcal{U}(0.0, 15.0)$	m s^{-1}	Amplitude of the dSHO-GP
$Q_0 \text{ GP, CARMENES-VIS}$	$\mathcal{J}(10^{-8}, 10^5)$...	Quality factor for the secondary oscillation of the dSHO-GP
$f_{\text{GP, CARMENES-VIS}}$	$\mathcal{U}(0.1, 1.0)$...	Fractional amplitude of the secondary oscillation of the dSHO-GP
$\delta Q_{\text{GP, CARMENES-VIS}}$	$\mathcal{J}(10^2, 10^8)$...	Quality factor difference between the first and second oscillations of the dSHO-GP
$P_{\text{rot, GP, CARMENES-VIS}}$	$\mathcal{U}(155.0, 175.0)$	d	Primary period of the dSHO-GP

Notes. The 90.3 d signal is not speculated to have planetary origins (Sect. 4.3), so we denote it as a signal “2”.

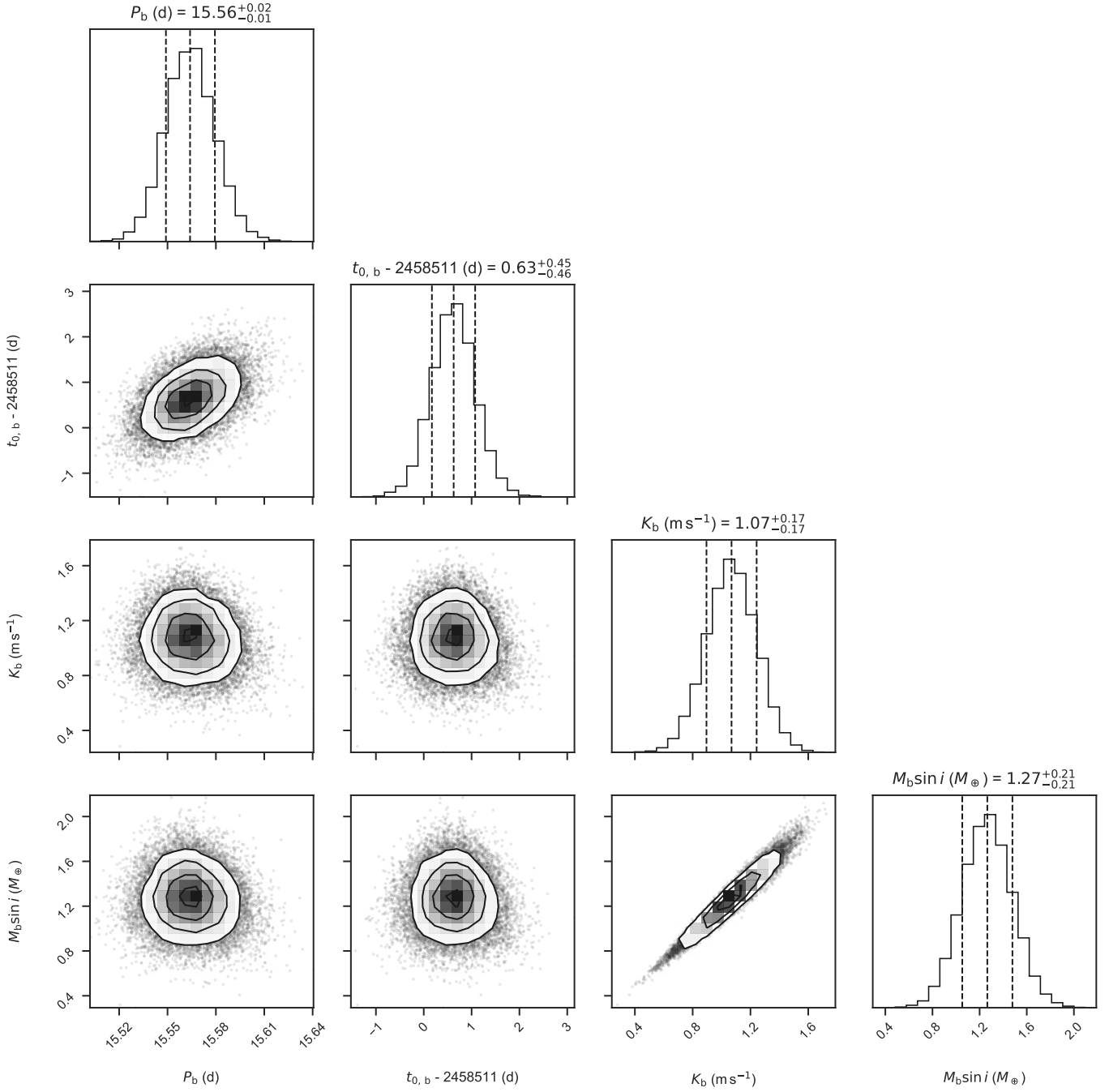


Fig. C.1. Posterior distributions for the inner-most planet Wolf 1069 b from the final RV fit described in Sect. 4.2.

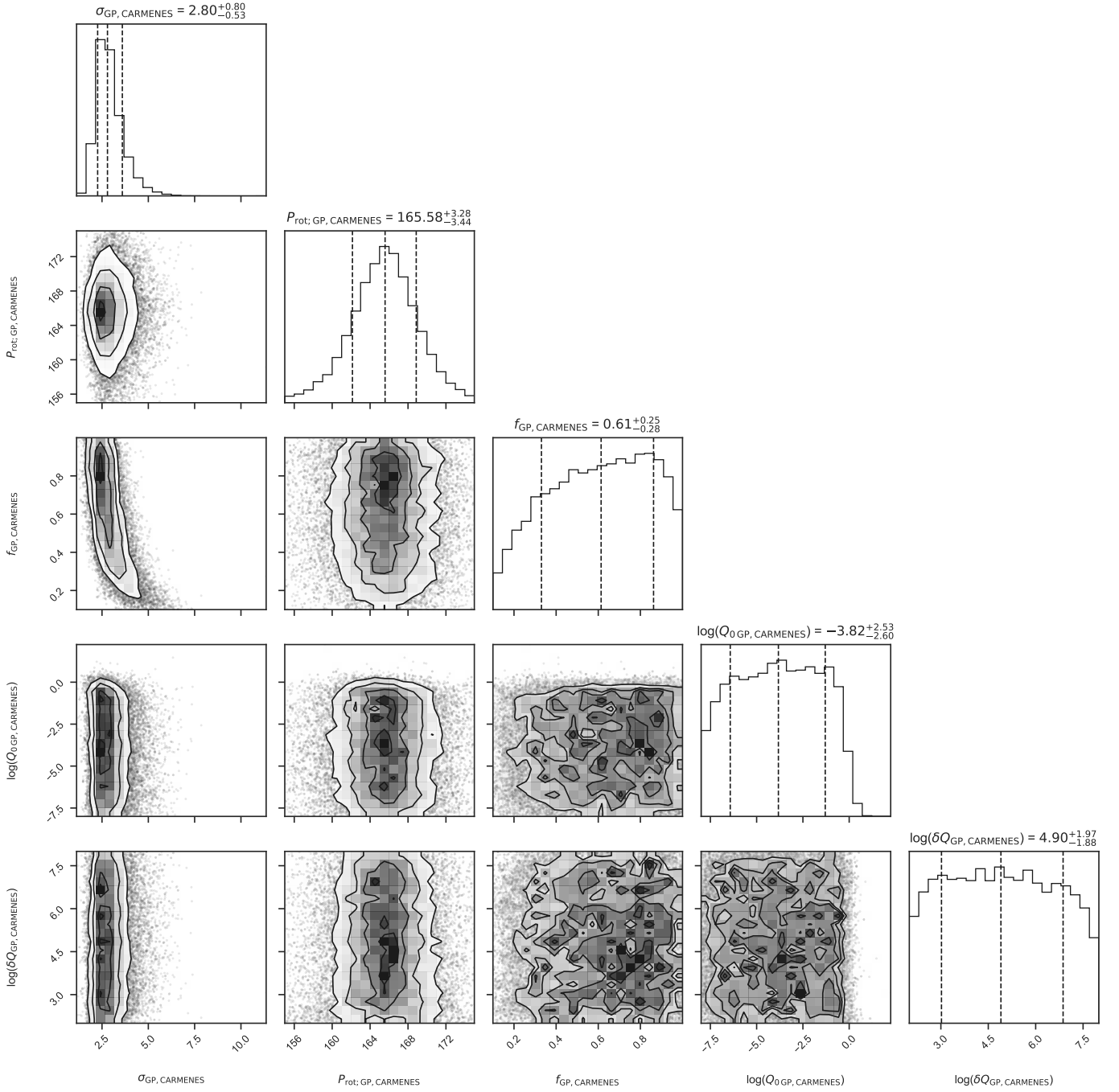


Fig. C.2. Posterior distributions for the stellar rotation period using the dSHO-GP from the final RV fit described in Sect. 4.2.

Table C.3. Full set of posterior parameters used in the final model choice for Wolf 1069 and described in Sect. 4.2.

Parameter	Posterior
<i>Posterior parameters for planet b</i>	
P_b	$15.564^{+0.015}_{-0.015}$
$t_{0,b}$	$2458511.63^{+0.45}_{-0.46}$
K_b	$1.07^{+0.17}_{-0.17}$
<i>RV instrumental parameters</i>	
$\gamma_{\text{CARMENES}} \text{ (m s}^{-1}\text{)}$	$-10.64^{+0.3}_{-0.39}$
$\sigma_{\text{CARMENES}} \text{ (m s}^{-1}\text{)}$	$0.47^{+0.36}_{-0.41}$
<i>dSHO-GP parameters</i>	
$\sigma_{\text{GP, CARMENES-VIS}}$	$2.80^{+0.80}_{-0.53}$
$Q_0 \text{ GP, CARMENES-VIS}$	$0.00015^{+0.05076}_{-0.00015}$
$f_{\text{GP, CARMENES-VIS}}$	$0.61^{+0.25}_{-0.28}$
$\delta Q_{\text{GP, CARMENES-VIS}}$	$80000^{+7300000}_{-78000}$
$P_{\text{rot, GP, CARMENES-VIS}}$	$165.6^{+3.3}_{-3.4}$

Table D.2. Telluric-corrected RV data used in this work for Wolf 1069. Data will be available online in machine-readable format.

BJD (TDB*)	RV (m s ⁻¹)	σ_{RV} (m s ⁻¹)	Instrument
2457563.66099	-11.183	1.547	CARMENES
2457569.58800	-10.331	3.441	CARMENES
2457575.61747	-12.551	1.584	CARMENES
2457584.59445	-15.557	2.250	CARMENES
2457591.51688	-11.028	1.915	CARMENES
2457594.58057	-14.606	2.152	CARMENES
2457596.52948	-15.083	1.468	CARMENES
2457597.44527	-16.279	1.138	CARMENES
2457610.51532	-13.451	1.577	CARMENES
2457612.45812	-12.912	1.810	CARMENES
2457613.43402	-12.103	1.540	CARMENES
⋮	⋮	⋮	⋮
2458978.65464	-12.167	2.433	CARMENES
2458988.61439	-9.675	1.770	CARMENES
2458994.61685	-9.450	1.428	CARMENES
2458999.63468	-6.863	1.591	CARMENES
2459000.64327	-7.105	1.278	CARMENES
2459001.64411	-7.717	1.318	CARMENES
2459006.64529	-5.812	1.641	CARMENES
2459010.59488	-5.312	1.664	CARMENES
2459015.61493	-7.113	1.513	CARMENES
2459017.64665	-9.772	3.050	CARMENES

Notes. (*) Barycentric dynamical time.

Appendix D: Short tables and data tables

Table D.1. Multiband photometry of Wolf 1069^a.

Band	Magnitude (mag)	Reference
B	15.82 ± 0.10	UCAC4
g'	14.78 ± 0.13	UCAC4
G_{BP}	14.368 ± 0.004	<i>Gaia</i> DR3
V	13.99 ± 0.05	UCAC4
r'	13.41 ± 0.05	UCAC4
i'	11.58 ± 0.09	UCAC4
G_{RP}	11.027 ± 0.004	<i>Gaia</i> DR3
J	9.029 ± 0.039	2MASS
H	8.483 ± 0.073	2MASS
K_S	8.095 ± 0.021	2MASS
$W1$	7.877 ± 0.023	AllWISE
$W2$	7.717 ± 0.020	AllWISE
$W3$	7.545 ± 0.016	AllWISE
$W4$	7.445 ± 0.084	AllWISE

Notes. ^(a) *Gaia* EDR3 G magnitude in Table 2.

References. 2MASS: [Skrutskie et al. \(2006\)](#); *Gaia* DR3: [Gaia Collaboration \(2023\)](#); UCAC4: [Zacharias et al. \(2012\)](#); WISE/AllWISE: [Cutri & et al. \(2012, 2014\)](#).